Electrostatic Atomization of Vegetable Oils with Single and Multi-Orifice Nozzles

by

PAUL WILLIAM VESELY
B.S., University of Illinois at Chicago, 2013

Thesis submitted in partial fulfillment of the requirements
for the degree of Master of Science in Mechanical Engineering
in the Graduate College of the
University of Illinois at Chicago, 2017

Chicago, Illinois

Defense Committee:
Farzad Mashayek, Chair and Adviser
Alexander Yarin
John Shrimpton, University of Southampton, UK, Co-Adviser

This thesis is dedicated to my wife, Emilee Johnson, without whom it would never have been accomplished.

ACKNOWLEDGMENTS

I would like to acknowledge and thank Dr. Mashayek and Dr. Shrimpton for being my advisers throughout my master's research project and for being on my thesis committee. Additionally, I would like to thank Dr. Yarin for being on my thesis committee. Their unwavering support, assistance, and guidance in all areas of this project helped me accomplish my research goals and enjoy myself in the process. I would like to acknowledge Rudolf Schick and Spraying Systems Company for sponsoring my project and for providing the laboratory space, equipment, and resources to perform the research for this thesis. Additionally, I would like to acknowledge and thank Rudolf Schick and Spraying Systems Co. for allowing me the opportunity to participate in their work-study program while pursuing my master's degree. The experience gained while simultaneously taking graduate courses, conducting research, and adding to my work experience and skills was immensely beneficial to my development as an engineer and my graduate education experience.

PWV

TABLE OF CONTENTS

TABLE OF CONTENTS (Continued)

CHAPTER **PAGE**

LIST OF TABLES

LIST OF FIGURES

LIST OF FIGURES (Continued)

LIST OF FIGURES (Continued)

FIGURE **PAGE**

LIST OF ABBREVIATIONS

B	$[T]$	Magnetic Field
$c = 2.998 \times 10^{8}$	$[m/s]$	Speed of Light in a Vacuum
D_d	$[m^2/s]$	Ionic Diffusion Coefficient
D_V	$[\mu m]$	Volume Diameter
d	$[m]$	Orifice Diameter
E	$[V/m]$	Electric Field
$e = 1.602 \times 10^{-19}$	$[C]$	Elementary Charge
$\vec{f}$	$[N]$	Force
$g = 9.81$	$[m/s^2]$	Gravity
I	$[A]$	Current
$\hat{i}$		Unit Vector
j	$[A/m^2]$	Current Flux
$k_b = 1.3806 \times 10^{-23}$	$[m^2kg/s^2K]$	Boltzmann Constant
L	$[m]$	Inter-Electrode Gap Length
l	$[m]$	Length
n	$[1/m^3]$	Number Density
p	$[Pa]$	Pressure
Q	$[C/kg]$	Mass Charge Density
Q_V	$[m^3/s]$	Volumetric Flow Rate

LIST OF ABBREVIATIONS (Continued)

q	[C]	Electric Charge
q_v	[C/m^3]	Space Charge or Spray Specific Charge
T	[K]	Temperature
t	[s]	Time
u	[m/s]	Velocity
U	[J/m^3]	Energy Density
V	[V]	Voltage
x, y, z, r	[mm]	Position

Greek

α	[1/K]	Thermal Expansion Coefficient
ε	[F/m]	Permittivity
$\varepsilon_o = 8.854 \times 10^{-12}$	[F/m]	Permittivity of Free Space
ε_r		Relative Permittivity
η		Atomizer Efficiency
κ	[m^2/Vs]	Ion Mobility
λ_d	[m]	Debye Length
μ	[P]	Dynamic Viscosity
μ_m	[H/m]	Permeability
ν	[St]	Kinematic Viscosity
$\pi = 3.1416$		Ratio of the Circumference to the Diameter of a Circle

LIST OF ABBREVIATIONS (Continued)

ρ	$[kg/m^3]$	Density
τ	[s]	Timescale Constant

Dimensionless Parameters

C	Injection Strength Parameter
Fr	Froude Number
Gr	Grashof Number
M	Mobility Parameter
Ra	Rayleigh Number
Re	Reynolds Number
T	Electric Rayleigh Parameter

Acronyms

EHD	electrohydrodynamic
HSI	high-speed imaging
HVPS	high voltage power source
LSI	laser sheet imaging
PDI	phase Doppler interferometry

SUMMARY

An electrostatic atomization nozzle was investigated to determine the viability of using this technology with soybean oil for industrial oil coating processes. The nozzle was constructed with a blunt high voltage electrode producing a plane-to-plane electrostatic atomization nozzle. Testing was conducted for various nozzle geometries including multiple inter-electrode gap distances, orifice diameters, and number of orifices. These nozzle variations were tested at two flow rates (jet velocities) for electrical performance and spray plume characterization. The motivation for testing a multi-orifice version of this nozzle was to increase the oil throughput for the nozzle and spray coverage. The increased capacity of the multi-orifice nozzle would provide more opportunity for the electrostatic atomization system to replace other nozzle technology currently in place for oil coating processes.

It was found that this nozzle design works well for the single orifice configuration with soybean oil. The single orifice nozzle produced spray specific charge results similar to previous research with soybean oil. This nozzle with soybean oil also produced similar drop size statistics compared to previous research with kerosene and diesel oil, which have much lower viscosity than soybean oil. This suggests that atomization mechanism of bending and Rayleigh instability is independent of the viscosity of the oil as far as the resulting drop size distribution is concerned.

The multi-orifice designs of the electrostatic atomization nozzle proved to be challenging and not consistent. Unexpected arcing occurred in the triangular region between the three orifices. Even with all three of the orifices residing well within the outer diameter of the high voltage

electrode, balanced charging did not always occur between the three oil jets resulting in narrow spray plumes among wide vigorously atomized spray plumes. However, it was successfully operated and met the goals of increasing the flow rate and spray coverage produced by the nozzle. Some further design refinements could alleviate the challenges encountered with this nozzle during this investigation.

CHAPTER 1

INTRODUCTION AND MOTIVATION

Electrostatic atomization nozzles have been studied by many researchers in the past decades. Electrohydrodynamics is an attractive method to atomize dielectric fluids with high viscosity, like oils. Traditionally, these are atomized via high hydraulic pressure or with the assistance of a compressed atomization gas. Both methods can generate small droplets but with the high energy cost associated with pumping or compressing the liquid and atomization gas, respectively. Heating of the oil before spraying is a typical process in industry to reduce the viscosity of the fluids to produce smaller droplets with lower atomization pressures or to improve spray pattern quality. Electrohydrodynamic atomization can generate finely atomized droplets with only milliwatts of electrical power consumption, with the added benefit of the charged droplets seeking for and collecting onto electrically grounded targets resulting in a very high transfer efficiency. Poor transfer efficiency is a common problem is traditional industrial oil coating processes.

The motivation for the work detailed in this thesis is to develop an electrostatic atomization nozzle for industrial oil coating processes. Industrial oil coating processes would greatly benefit from charged, targeted sprays resulting in high transfer efficiency. The nozzle requires further development and testing to increase flow rate, spray coverage, and reliability to work for an industrial process at the conveyor speeds currently being used for oil coating applications.

The majority of work conducted by previous researchers was related to electrostatically atomizing fuels for combustion processes. For this thesis, the work focused on studying how technology designed for spraying low viscosity fuels like diesel and jet fuels works with higher viscosity vegetable oils building on the research started by Malkawi (formerly Al-Ahmad) (1). Malkawi investigated the electrical performance of the electrostatic atomization nozzle with various electrode designs with the hydrocarbon-based fuels of diesel and JP8 and with the vegetable oils of corn and soybean oil. Malkawi also investigated the electrical performance of multi-orifice configurations of the electrostatic atomization nozzle with various electrode shapes with diesel fuel only.

For this thesis, experiments were conducted on single and multi-orifice electrostatic atomization nozzles spraying soybean oil. The electrical performance of these nozzles was tested and compared to Malkawi's results to validate the nozzle used and the experimental setups. New contributions to the study of electrostatic atomization nozzles consisted of characterizing the spray plume generated by the single and multi-orifice electrostatic atomization nozzle spraying soybean oil via various imaging techniques including high-speed imaging, laser sheet imaging, and phase Doppler interferometry. Drop size distribution results for the single orifice electrostatic atomization nozzle were compared to results for kerosene conducted by Shrimpton and Yule (2). Various nozzle geometries including the inter-electrode gap, orifice diameter, and number of orifices were investigated to see how they impact the spray plume generated by the nozzle. The structure of the thesis begins with a literature and theoretical review, followed by

the presentation of the various experimental setups used, followed by experimental results and analysis, and ending with the conclusions and recommended future work.

CHAPTER 2

LITERATURE REVIEW

2.1 Previous Work

Electrohydrodynamics is the study of how electric fields impact fluid motion. Some of the earlier work on this phenomenon was conducted by Melcher and Taylor (3). They did an experiment that demonstrated that electroconvection could be induced in corn oil with selective positioning of the high voltage and ground electrodes. The development of EHD nozzles began with Kim and Turnbull (4) who used a needle electrode in a capillary glass tube to electrostatically spray Freon 113. This nozzle design generated spray currents on the order of nanoamps and droplets on the order of 10 microns at very low flow rates. A nozzle for electrospraying uses only one electrode within the nozzle and the spray target is the ground electrode. Testing of the electrospraying nozzle continued with Robinson et al. (5). They sprayed silicone oil with the same style nozzle and showed that more resistive fluids could be atomized with the electrospraying nozzle and verified that atomization occurs at lower voltages if the high voltage electrode has a negative polarity versus a positive polarity.

A spray triode nozzle was developed by Kelly (6) to improve on the single electrode version developed by Kim and Turnbull (4). The spray triode nozzle contains three electrodes; the high voltage electrode in the center of the nozzle, a ground electrode plate with holes in the bottom of the nozzle close to the high voltage electrode, and a ground electrode attached to

the outside of the nozzle. This nozzle design brought the high voltage and ground electrodes close together to generate stronger charging of the oil and allowed for the nozzle to operate at higher flow rates. The body of the nozzle was made of a dielectric material. The third electrode outside the body nozzle was grounded and was used to assist in drawing the charged fluid out of the nozzle. The high voltage electrode in this nozzle was a sharp point electrode making a point-to-plane electrode arrangement.

The spray triode nozzle was further improved upon by Yule et al. (7). In this design, the needle high voltage electrode was located within a conducting nozzle body, which made up the ground electrode. No third electrode was connected to the nozzle. Instead, the target being sprayed was grounded and attracted the charged spray. This nozzle was investigated with various hydrocarbon fluids like diesel oil, kerosene, and white spirit. This nozzle contained a large orifice diameter of 500 microns and had a large inter-electrode gap and orifice length. It produced an atomized spray but with low spray specific charge, which was typically under 1 C/m^3. This nozzle became known as the 1st generation atomizer.

The 2nd generation electrostatic atomization nozzled designed by Shrimpton and Yule (2) simplified the body of the nozzle to focus on the electric field instead of the fluid flow path through the nozzle. This new design allowed for the needle high voltage electrode to be much closer to the nozzle body and orifice and smaller orifice diameters were tested. With this nozzle design, they were able to achieve spray specific charge levels up to 3 C/m^3 (8).

The 3rd generation electrostatic atomization nozzle designed by Rigit and Shrimpton (9) was very similar to the previous version except it included a PTFE guide to keep the needle

high voltage electrode centered with the orifice to maximize the electric field strength at the charging region of the nozzle. This nozzle was used in subsequent studies with various types of high voltage electrodes and for multi-orifice testing. This atomizer design was used for this research.

The single orifice electrostatic atomization nozzle is limited to the maximum orifice diameter and flow rate it can operate at. When the electric field of the jet of fluid exiting the nozzle reaches a critical value, partial breakdown or supercritical breakdown condition occurs and the nozzle stops atomizing (10). At this condition, the electric field is strong enough to generate corona discharge in the air surrounding the jet of oil that exits the nozzle (11). The maximum electric field strength achievable before partial breakdown condition occurs is related to the inverse proportional relationship between the jet diameter and the spray specific charge as

$$E = \frac{q_v d}{4\epsilon_r \epsilon_0} \tag{2.1}$$

Since the orifice diameter has to remain small for the liquid jet exiting the nozzle to carry enough charge to generate atomization, multi-orifice nozzle designs were explored by Malkawi (1). The purpose of this research was to increase the flow rate of oil that could be atomized via an electrostatic atomization nozzle. This research studied various high voltage electrode types as the point electrode is limited to working with a single orifice. He found that the blunt electrode making up a plane-to-plane electrostatic atomization nozzle resulted in the highest spray specific charge with multiple orifices arranged in a circular array.

Further investigation of the multi-orifice electrostatic atomization nozzle was conducted by Kourmatzis et al. (12). The purpose of this testing was to see if high levels of spray specific charge could be obtained if point or needle electrode was used for each orifice within the multi-orifice nozzle. Instead of trying to align an array of needle electrodes with an array of orifices, they made a diamond-encrusted blunt electrode. This resulted in the maximum spray specific charge being obtained at lower operating voltages.

More recently, the EHD nozzle has been investigated for pulsed sprays by Kourmatzis (13) and for remote charging of the fluid and high pressure sprays by Ergene (14). Neither of these applications was explored in this thesis.

2.2 Theoretical Review

An electrostatic atomization nozzle was built for the testing in this thesis based on the design of the 3rd generation atomizer by Rigit and Shrimpton (9). A blunt electrode was used in this nozzle in place of the needle electrode in the original design based on the studies by Malkawi (1) showing that the blunt ended electrode produced higher levels of spray specific charge at lower nozzle operating voltages. With the use of a blunt electrode in this generation of an atomizer, a plane-to-plane electrohydrodynamic environment will be in place between the electrode and the body of the nozzle. The mathematical and physical model representing the charging process for a plane-to-plane system will be reviewed in this section. The geometry to be modeled is the simple case of a dielectric fluid in between two plates. One plate is the high voltage electrode and the other a grounded collecting plate. The theoretic review will begin with

some definitions and equation for electrostatics and then will move into electrohydrodynamics and the Navier-Stokes equations. Lastly, important non-dimensional parameters will be defined.

2.2.1 Permittivity

Permittivity relates to a materials ability to transmit an electric field. It is a function of the material's molecular structure and the degree of freedom of the elecrons (15). The relative permittivity, ε_r is related by the material permittivity, ε, and the permittivity of free space, ε_o, by

$$\varepsilon_r = \frac{\varepsilon}{\varepsilon_o}. \tag{2.2}$$

The permittivity of free space is the permittivity of a vacuum where all charges are free to act on one another and is used as a reference value when determining relative permittivity.

2.2.2 The Coulomb Force and Gauss's Law

The presence of charges in the fluid generates electrical forces and influence the electric field in the spray. Charged particles are of two basic types, monopoles, and dipoles. Monopoles consist of a single charge whereas a dipole consists of two equal but opposite charges. Coulomb's Law describes the force between two static monopoles, q_1 and q_2 and is shown as

$$\vec{f}_{i,1} = \frac{q_1 q_2}{4\pi\varepsilon \left|x_{i,1} - x_{i,2}\right|^2} \hat{i}_{i,21}. \tag{2.3}$$

In this equation, $x_{i,1}$ and $x_{i,2}$ represent the locations of charges q_1 and q_2 respectively and $\hat{\imath}_{i,21}$ is the unit vector from q_2 and q_1. This gives the force on q_1 from q_2. A generalized form of Equation 2.3 showing the force on a charge from many charges is

$$\vec{f}_{i,1} = q\vec{E}_i, \tag{2.4}$$

where

$$\vec{E}_i = \sum_m \frac{q_m}{4\pi\varepsilon \left|x_{i,1} - x_{i,m}\right|^2} \hat{\imath}_{i,m1}. \tag{2.5}$$

The relation of the electric field, $\vec{E}_i$, generated by the surrounding charges is called Gauss's Law. Gauss's Law relates the instantaneous electric field to the space charge or charge density, q_v at any point in the continuum. The differential form of Gauss's Law is shown as

$$\frac{\partial E_i}{\partial x_i} = \frac{\rho Q}{\varepsilon} = \frac{q_v}{\varepsilon}. \tag{2.6}$$

2.2.3 Dielectrics and Polarization

The electrical nature of a material can be classified into two classes, conductors and dielectrics or insulators. In a conductor, like metals, electrons are free to move about the crystal structure of the material allowing a flow of charge when an electric field is applied. In an insulator, electrons are bound to their atoms or molecules. A perfect insulator would be a medium in which no charge would flow meaning that the medium has infinite resistivity. When an electric field is applied to a dielectric medium, charge carriers are restricted from moving indefinitely

due to their bond with their atom or molecule, and instead, the positive charge carriers align with the electric field and the negative charge carriers against creating the polarized state.

2.2.4 Electroquasistatic Assumptions

The electroquasistatic assumption states that the electrical energy is much greater than the magnetic energy resulting in magnetic energy effects being ignored (16). Electrical and magnetic energy densities are respectively defined by the following:

$$U_e = \frac{1}{2}\varepsilon E^2 \tag{2.7}$$

$$U_b = \frac{1}{2}\frac{B^2}{\mu_m} \tag{2.8}$$

To satisfy the electroquasistatic assumption, the ratio of electrical to magnetic energy densities must be much greater than one, shown as

$$\frac{(\varepsilon E^2)/2}{B^2/(2\mu_m)} = \frac{E^2}{c^2 B^2} \gg 1. \tag{2.9}$$

As a result of the electroquasistatic assumption, the general Maxwell equations reduce to the following:

$$\nabla \times \vec{E} = 0 \tag{2.10}$$

$$\nabla \cdot \vec{E} = \frac{q}{\varepsilon} \tag{2.11}$$

$$\frac{\partial q}{\partial t} + \nabla \cdot \vec{J} = 0 \tag{2.12}$$

2.2.5 Mobility and Charge Transport

Several factors affect the transport of charge in a dielectric liquid medium. The first is the transport of charge, or current flux, by the convective bulk motion of the liquid (15) shown as

$$j_i = q_v u_i. \tag{2.13}$$

In this equation, the velocity, u_i, is known as the ionic drift velocity which is defined as

$$u_i = \kappa E_i, \tag{2.14}$$

and is the terminal velocity of the charge in the medium. The ionic mobility, k, in an insulating fluid is related to the fluid's viscosity by Walden's Rule (15) and is shown as

$$\kappa_n = \frac{3 \times 10^{-11}}{\mu}, \kappa_p = \frac{1.5 \times 10^{-11}}{\mu}, \tag{2.15}$$

where κ_n is ionic mobility for negative polarity charging, κ_p is for positive polarity charging, and μ is the viscosity of the insulating fluid. The ionic mobility is defined as the relationship between the electric field applied and the terminal velocity of a charge (13). Using Equation 2.14, the current flux can be rewritten and be defined as the ionic drift equation given by

$$j_i = q_v \kappa E_i. \tag{2.16}$$

Charge carriers also travel by diffusion into the dielectric fluid. The Debye length is the thickness of this diffusion area around an electrode and is defined by

$$\lambda_d = \left(\frac{\varepsilon k_b T}{n e^2} \right)^{1/2}, \tag{2.17}$$

where n represents the number density of charge carriers. The current flux due to diffusion is shown as

$$j_i = -D_d \frac{\partial q_v}{\partial x_i}, \tag{2.18}$$

where D_d is the ionic diffusion coefficient given by the Einstein relation (15) shown as

$$D_d = \frac{\kappa k_b T}{e}, \tag{2.19}$$

where T is temperature, k_b is the Boltzmann constant and e is the elementary charge.

Charge conservation is the principle that electric charge cannot be created or destroyed. Summing the three current flux equations together and using the scalar transport Equation 2.12 (15), we get the following:

$$j_i = q_v \kappa E_i - D_d \frac{\partial q_v}{\partial x_i} + q_v u_i. \tag{2.20}$$

$$\frac{\partial q_v}{\partial t} + \frac{\partial j_i}{\partial x_i} = 0. \tag{2.21}$$

2.2.6 Conservation of Mass and Momentum

The Navier-Stokes equations for mass and momentum of classical fluid mechanics are modified to introduce the effects of the electrical forces on the fluid. The one-dimensional, incompressible version of the Navier-Stokes equations will be explored for this application of electrohydrodynamics. For the conservation of mass, the effect of electrical forces does not result in the addition of any new terms to the equation used for classical fluid mechanics, and is shown as

$$\frac{\partial u_i}{\partial x_i} = 0. \tag{2.22}$$

For the conservation of momentum,

$$\rho\frac{\partial u_i}{\partial t} + \rho u_j\frac{\partial u_i}{\partial x_j} = -\frac{\partial p}{\partial x_i} + \mu\frac{\partial^2 u_i}{\partial x_j^2} + \rho g_i + f_i, \tag{2.23}$$

a new term, f_i, is added to include the effect of the electrical force due to the electrical charge present in the fluid. This new term represents the volume electrical force for a linear medium (15), and is shown as

$$f_i = q_v E_i - \frac{1}{2}E^2\frac{\partial}{\partial x_i}\varepsilon + \frac{1}{2}\frac{\partial}{\partial x_i}\left[\rho\left(\frac{\partial \varepsilon}{\partial \rho}\right)_T E^2\right]. \tag{2.24}$$

The leftmost term is Equation 2.4, Gauss's Law, and is the most dominant term of the three. The middle term is called the dielectric force and is significant in alternating electric fields with a cycle significantly smaller than the charge relaxation or ionic transit time (16). The right

term is the electrostrictive pressure and may be grouped with the standard pressure term in the conservation of momentum equation.

2.2.7 Electrical Timescales

There are many timescales associated with Electrohydrodynamics with many interpretations depending on the application. These timescales aid in defining the various processes that occur within a electrostatic atomizer. To define these time scales, reference values for length l_o, velocity u_o, charge density q_{vo}, voltage V_o, and electric field E_o will be used. With the assumption that the dielectric fluid is incompressible and ignoring temperature effects, the density ρ and viscosity μ of the dielectric medium are considered reference values (15).

The space charge relaxation timescale is defined by

$$\tau_{sc} = \frac{\varepsilon}{q_{vo}\kappa}, \tag{2.25}$$

and characterizes the rate which charge decays from a given source (15). With the space charge being on the bottom of this ratio, a smaller initial space charge will decay more slowly than a large one.

The ionic diffusion timescale is relevant close to the high voltage electrode where a thin layer of ion diffusion occurs. In this layer, an electrochemical reaction occurs which produces

the charge carriers in the fluid (13). The electrochemical reaction appears to be due to faradic reactions at the electrodes (17). The ionic diffusion timescale is given by

$$\tau_d = \frac{D_d}{\lambda_d^2}. \tag{2.26}$$

The ionic transit timescale is the proportion of the characteristic length of the electrohydrodynamic process to the drift of ions (15) and is shown as

$$\tau_\kappa = \frac{l_o^2}{\kappa V_o}. \tag{2.27}$$

This timescale is of a higher relevance than the ionic diffusion timescale if the bulk flow convection is being studied away from the electrode.

The electro-viscous timescale compares viscous forces to electrical forces given by

$$\tau_{ev} = \frac{\mu}{\varepsilon E_o^2}. \tag{2.28}$$

This timescale describes how quickly a liquid accelerates to a constant after the voltage is initially applied to the electrode (15).

The electro-inertial timescale compares the inertial forces to the electrical forces. This timescale describes the time taken for the fluid to travel the characteristic length due to an

electric pressure (13). This timescale is relevant when inertial and electrical forces are of the same order of magnitude (15). The electro-inertial timescale is given by

$$\tau_{ei} = l_o \sqrt{\frac{\rho}{\varepsilon E_o^2}}. \tag{2.29}$$

Two non-electrohydrodynamic timescales are essential to the equations to be discussed in the next subsection. They are the mechanical and viscous timescales. The mechanical timescale given by

$$\tau_m = \frac{l_o}{u_o}, \tag{2.30}$$

which relates the reference length to the reference velocity. The viscous timescale,

$$\tau_\nu = \frac{\rho_o l_o^2}{\mu_o}, \tag{2.31}$$

represents the time needed for the velocity gradient to develop within the moving liquid (13).

2.2.8 Conservation of Momentum in the Non-Dimensional Form

To transform the conservation of momentum Equation 2.23 into its non-dimensional form, the same reference quantities mentioned in the previous subsection for the timescales will be used. The scaling factors used are the following:

$$x^* = \frac{x}{l_o} \ , \ u^* = \frac{u}{\kappa E_o} \ , \ q_\nu^* = \frac{q_\nu}{q_{\nu o}} \ , \ p^* = \frac{p}{\rho u_o^2}. \tag{2.32}$$

Dividing through by density and applying the scaling these scaling factors, the conservation of momentum for free flow is transformed into (15)

$$\begin{aligned}\frac{\partial u_i^*}{\partial t^*} + u_j^* \frac{\partial u_i^*}{\partial x_j^*} = -\frac{p_o}{\rho u_o^2}\frac{\partial p^*}{\partial x_i^*} + \frac{\nu}{\kappa V_o}\frac{\partial^2 u_i^*}{\partial x_j^{*2}} + \frac{g_o l_o^3}{\kappa^2 V_o^2} g_i^* \\ + \left(\frac{q_{vo} l_o^2}{\rho \kappa^2 V_o}\right) q_v^* E_i^* - \left(\frac{\varepsilon_o}{\rho\kappa^2}\right)\frac{1}{2} E^{*2}\frac{\partial}{\partial x_i^*}\varepsilon^* + \left(\frac{\varepsilon_o}{\rho\kappa^2}\right)\frac{1}{2}\frac{\partial}{\partial x_i^*}\left[\rho\left(\frac{\partial \varepsilon^*}{\partial \rho}\right)_T E^{*2}\right].\end{aligned} \tag{2.33}$$

The reference velocity is given by the ionic drift velocity κE.

In transforming this equation into its non-dimensional form, important non-dimensional parameters are produced. Introducing non-dimensional parameters transforms the conservation of momentum equation as (13)

$$\begin{aligned}\frac{\partial u_i^*}{\partial t^*} + u_j^* \frac{\partial u_i^*}{\partial x_j^*} = -\frac{\partial p^*}{\partial x_i^*} + \frac{1}{Re_E}\frac{\partial^2 u_i^*}{\partial x_j^{*2}} + \frac{1}{Fr_E} g_i^* \\ + CM^2 q_v^* E_i^* - M^2 \frac{1}{2} E^{*2}\frac{\partial}{\partial x_i^*}\varepsilon^* + M^2\frac{1}{2}\frac{\partial}{\partial x_i^*}\left[\rho\left(\frac{\partial \varepsilon^*}{\partial \rho}\right)_T E^{*2}\right].\end{aligned} \tag{2.34}$$

The same dimensional analysis can be performed to produce the non-dimensional form of the conservation of momentum for forced flows. For forced flows, the characteristic velocity is the bulk fluid velocity of the system (15). This results in the following:

$$\begin{aligned}\frac{\partial u_i^*}{\partial t^*} + u_j^* \frac{\partial u_i^*}{\partial x_j^*} = -\frac{p_o}{\rho u_o^2}\frac{\partial p^*}{\partial x_i^*} + \frac{\nu}{u_o l_o}\frac{\partial^2 u_i^*}{\partial x_j^{*2}} + \frac{g_o l_o}{u_o^2} g_i^* \\ + \left(\frac{q_{vo} V_o}{\rho u_o^2}\right) q_v^* E_i^* - \left(\frac{\varepsilon_o V_o^2}{\rho u_o^2 l_o^2}\right)\frac{1}{2} E^{*2}\frac{\partial}{\partial x_i^*}\varepsilon^* + \left(\frac{\varepsilon_o V_o^2}{\rho u_o^2 l_o^2}\right)\frac{1}{2}\frac{\partial}{\partial x_i^*}\left[\rho\left(\frac{\partial \varepsilon^*}{\partial \rho}\right)_T E^{*2}\right]\end{aligned} \tag{2.35}$$

$$\frac{\partial u_i^*}{\partial t^*} + u_j^* \frac{\partial u_i^*}{\partial x_j^*} = -\frac{\partial p^*}{\partial x_i^*} + \frac{1}{Re}\frac{\partial^2 u_i^*}{\partial x_j^{*2}} + \frac{1}{Fr} g_i^* + \frac{Gr_E}{Re^2} q_v^* E_i^* - \frac{T^2}{Re^2 M^2}\frac{1}{2} E^{*2}\frac{\partial}{\partial x_i^*}\varepsilon^* + \frac{T^2}{Re^2 M^2}\frac{1}{2}\frac{\partial}{\partial x_i^*}\left[\rho\left(\frac{\partial \varepsilon^*}{\partial \rho}\right)_T E^{*2}\right] \tag{2.36}$$

2.2.9 Important Non-Dimensional Parameters

In the previous subsection, many important non-dimensional parameters appeared in the equations. The classical Reynolds and Froude numbers appeared in the forced flow form of the conservation of momentum equation and are defined respectively by the following:

$$Re = \frac{u_o l_o}{\nu} \tag{2.37}$$

$$Fr = \frac{u_o}{\sqrt{g_o l_o}} \tag{2.38}$$

In the free flow version of the non-dimensional conservation of momentum equation, a new version of these numbers is present and are called the electrical Reynolds and electrical Froude numbers. The electrical Reynolds number,

$$Re_E = \frac{\kappa V_o}{\nu} = \left(\frac{\mu\kappa}{\varepsilon_o V_o}\right)\cdot\left(\frac{\varepsilon_o}{\rho\kappa^2}\right) = \frac{T}{M^2}, \tag{2.39}$$

is the proportion of the ionic drift to the viscosity timescales (15).

The electrical Grashof number is defined by the proportion of the Coulombic to the viscous body forces (15). The electrical Froude number is given as

$$Gr_E = \frac{q_{vo} V_o l_o^2}{\mu \nu}. \tag{2.40}$$

The stability of an electrostatic atomization system is measured by the T parameter, which is also known as the electric Rayleigh parameter. (15). This number is used to quantify the instability in an electroconvective problem. It is used to define when a system goes from pure conduction to convection and then to turbulent convection. In electrohydrodynamics, the value of T where electroconvective roll structure begins to appear is known as the critical stability parameter, T_c (13). The T parameter is given by

$$T = \frac{\varepsilon V_o}{\mu \kappa} = M^2 Re_E. \tag{2.41}$$

For an idle fluid with a strong injection case, electroconvective roll begins at $T \geq 99$ and is known as the minimum stability criteria (15). The electrical Rayleigh parameter is analogous to Rayleigh-Benard convection where a $Ra > 1708$ is required for heat transfer before conduction turns into convection for the same geometry being studied for this electroconvective process (13).

The T parameter has been related to the electro-viscous timescale to represent the time for a charge carrier to travel from the electrode to the collecting electrode (13). This is called the transit timescale and is shown as

$$\tau_t \sim 2T\tau_{ev}. \tag{2.42}$$

The M parameter, known as the mobility parameter, is the proportion of the hydrodynamic to the ionic mobilities (18) and is given by

$$M = \frac{\sqrt{\varepsilon/\rho}}{\kappa}. \tag{2.43}$$

With the assumption that electrical energy is changed completely into kinetic energy, the maximum value for hydrodynamic mobility can be determined (15). The M parameter is related to the T parameter and the electrical Reynolds number by (19)

$$T = M^2 Re_E. \tag{2.44}$$

The C parameter is called the injection strength parameter and is given by

$$C = \frac{\tau_\kappa}{\tau_{sc}} = \frac{q_{vo} l_o^2}{\varepsilon V_o}. \tag{2.45}$$

This parameter is a ratio of the ionic drift timescale to the space charge relaxation time scale (15). The electric field within the fluid is due to the potential difference across the two plates for

weak charging systems from the present of charges in the fluid for strong charging systems(15). A more precise definition of the injection strength is given as the following (15):

$$\begin{aligned} &\text{Strong Injection:} && 5 < C < \infty \\ &\text{Medium Injection:} && 0.2 < C < 5 \\ &\text{Weak Injection:} && 0 < C < 0.2 \end{aligned}$$

Some recent work by Kourmatzis and Shrimpton (20) has introduced two new dimensionless parameters. The goal of this work was to link the charging process inside of the nozzle with the charged liquid jet outside of the nozzle. The jet Reynolds number,

$$Re_j = \frac{\rho u_j d}{\mu}, \tag{2.46}$$

is the ratio of inertial forces to viscous forces in the jet region of the fluid. The jet region is where the fluid is exiting the orifice of the nozzle. For the jet Reynolds number, u_j is the velocity of the fluid exiting the nozzle orifice, and d is the orifice diameter.

Kourmatzis and Shrimpton (20) also defined an electric jet Reynolds number,

$$Re_{E,j} = \frac{\rho \kappa q_v d^2}{\varepsilon \mu}. \tag{2.47}$$

For the electric jet Reynolds number, it is assumed that the electric field is proportional to $q_v d/\varepsilon$.

With these two new non-dimensional parameters, they propose two new constants which appear to be universal for electrostatic atomization systems irrespective of the liquid, nozzle geometry, or operating parameters (20). The first constant given as

$$\left(\frac{q_v d}{\varepsilon}\right)\left(\frac{1}{E}\right)\left(\frac{d}{L}\right) \sim 0.06, \tag{2.48}$$

which represents the proportion of jet to the inter-electrode gap electric fields multiplied by the geometrical non-dimensional factor d/L (20). The second constant given as

$$\left(\frac{\kappa E}{u_j}\right)\left(\frac{L}{d}\right) \sim 0.6 \tag{2.49}$$

signifies the proportion of ionic drift to the liquid jet velocities in between the electrodes, and multiplied by the inter-electrode gap distance L/d (20).

CHAPTER 3

EXPERIMENTAL SETUP

A schematic of the nozzle operation setup used in this study is shown in Figure 1. This was used throughout all of the experiments run for this thesis. A fluid delivery system was used to supply oil to the nozzle. A high voltage power source was used to charge the oil. The charged spray exiting the nozzle was collected in a grounded steel can lined with steel wool. Electrical circuits were constructed to ground and measure the current from the nozzle body and the spray collection can. All of these components are explained in detail in the subsequent sections.

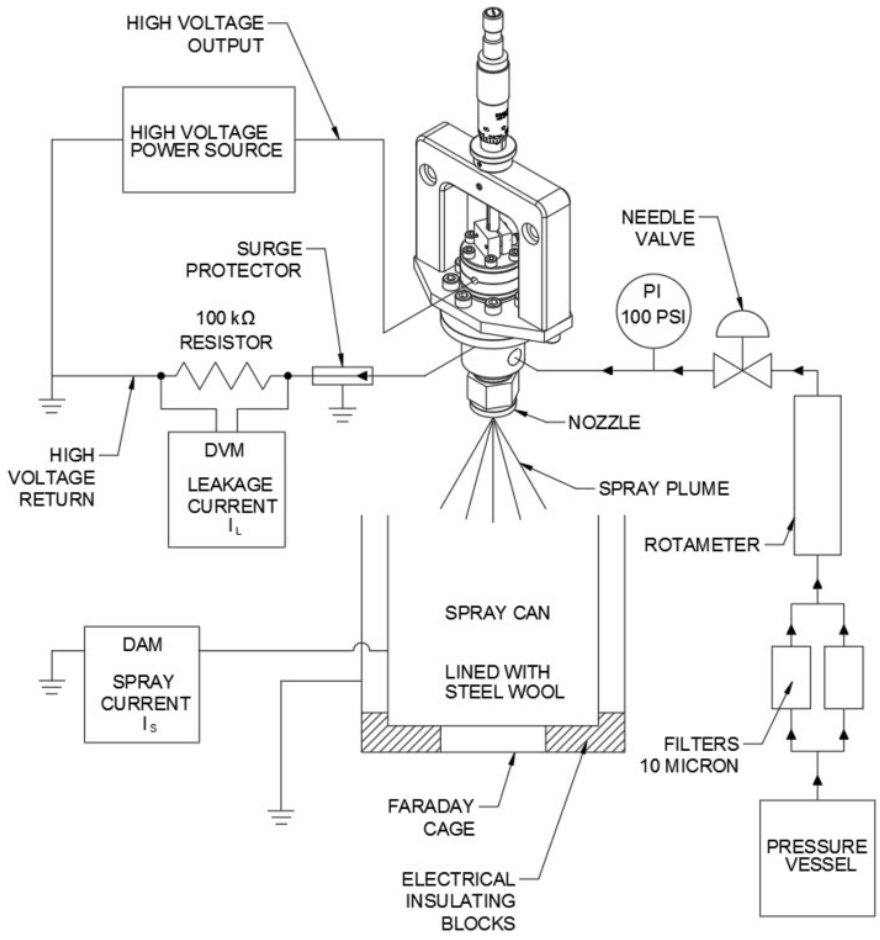

Figure 1. Schematic of the nozzle operation portion of the experimental setup.

3.1 Electrostatic Atomization Nozzle

The nozzle used in this study is based on the design of the 3rd generation electrostatic atomizer designed by Rigit and Shrimpton (9), and is shown in Figure 2. This design features

a guide for the electrode to keep it centered over the orifice and allows for the inter-electrode gap, L, to be easily adjusted. This adjustment is made using a micrometer head with a non-rotating spindle. The micrometer head used in this nozzle has a resolution of 0.0254 mm (0.001 in). Removable orifice plates attach to the bottom of the nozzle allowing the flexibility to easily test various orifice diameters, d, and multi-orifice configurations. These features are shown in the nozzle schematic shown in Figure 3. A blunt end tungsten rod with its sharp corners removed made up the high voltage electrode in this nozzle providing a plane-to-plane electrostatic atomization nozzle with the flat orifice disk. This design effectively makes a plane-to-plane capacitor with the orifice disk being the ground electrode and the oil as the dielectric medium.

Figure 2. The electrostatic atomization nozzle.

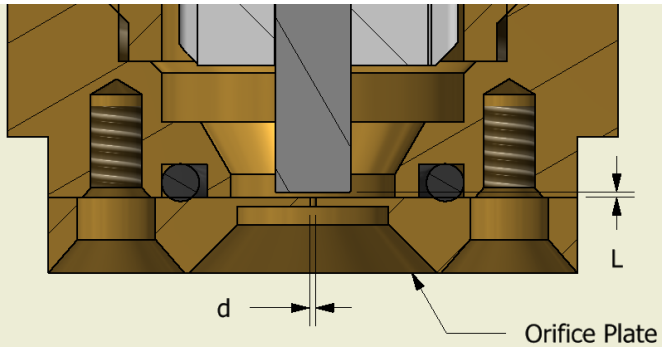

Figure 3. Section view of the electrostatic atomization nozzle showing the critical features of the inter-electrode gap, orifice, and removable orifice disks.

3.2 Electrical Circuits and Equipment

The major components of the electrical circuits used for all of the tests are shown in Figure 1. There are three electrical circuits in this test setup; the high voltage circuit, the leakage current circuit, and the spray current circuit. For the high voltage circuit, the primary piece of equipment was the Acopian N030HP1 high voltage power supply (HVPS), which was used in this experiment to charge the nozzle. This HVPS generates a negative polarity voltage adjustable between 0 to -30 kV with the current limited to 1 mA maximum. Since this power supply contains analog meters for display of the output voltage and current, two Falcon F35 digital panel meters were wired to the HVPS to monitor these outputs providing a resolution of 100 V and 0.1 mA respectively. These digital panel meters were assembled to a control panel along with potentiometers to adjust the output voltage and current, a high voltage output

on/off switch, and an emergency stop button. The high voltage output switch was necessary as the HVPS required a warm-up period of thirty minutes before testing. The switch allowed for the high voltage output to be turned off in between experiments so that the nozzle could be safely handled without shutting off the HVPS completely. The emergency stop button was wired to cut off the power supply to the HVPS if pressed. Silicone coated wire rated for 40 kVDC and high voltage connectors were used between the HVPS and the nozzle.

Figure 4. Acopian N030HP1 high voltage power source (top) with a custom built remote control panel (bottom).

The purpose of the leakage current circuit was two-fold; to measure the current leaking through the oil to the orifice disk and nozzle body, and to ground the orifice disk to the HVPS to complete the high voltage power supply circuit. This circuit consisted of a surge protector and a digital multimeter measuring the voltage across a 100 kΩ resistor. With the small inter-electrode gaps used in this study, $0.06 \leq L \leq 0.30$ mm, there was a risk of a catastrophic breakdown or arc between the two electrodes in the nozzle if dirt or air got in between them or if the voltage was too high. Attempting to measure the leakage current directly and without protection could lead to permanent damage to the digital multimeter when a catastrophic breakdown occurs. To protect against this, an MTL-Instruments CA90F surge protector was used to safely discharge the current from the electrical discharge to ground when the voltage spiked above 90 VDC. To further attempt to protect the digital multimeter from damage in the event of an electrical discharge, the voltage across a resistor was measured instead of directly measuring the current.

The spray current circuit consisted of a steel can lined with steel wool surrounded by a grounded cage. The grounded cage acted as a Faraday cage to isolate the spray current generation source from outside RF noise, which resulted in steady spray current measurements. The spray can was grounded back to the HVPS using a shielded cable wire. A BK Precision 2831E digital multimeter, with a resolution of 0.1 μA, was used to measure the spray current directly in this circuit.

3.3 Fluid Circuit and Equipment

The schematic in Figure 1 shows all of the major components of the fluid circuit. A pressure vessel was used to deliver oil to the nozzle. The oil was filtered with two bronze porous filters for capturing particulates as small as 10 microns. These were assembled in the fluid circuit in parallel to reduce the overall pressure drop across the filters. A 150 mm scale rotameter style flow meter, with 1 mm resolution, was used to measure the volumetric flow rate of the oil. A high precision needle valve was used to control the oil flow rate to the nozzle. A digital pressure gauge was used to measure the pressure at the fluid inlet of the nozzle. This pressure gauge had a range of 0 to 100 psig (0 to 6.9 barg) with a resolution of 0.1 psi.

In order to measure the volumetric flow rate of the soybean oil passing through the nozzle, the rotameter had to be calibrated. This was done by taking timed mass collections for the oil at different heights on the rotameter scale. These timed mass collections were repeated three times at each height on the rotameter and averaged. Using the density of the soybean oil tested, a plot of the volumetric flow rate versus rotameter height was produced, which can be found in Figure 5. A second order polynomial was fit to this data and used to relate flow rate to the rotameter height when operating the nozzle with soybean oil.

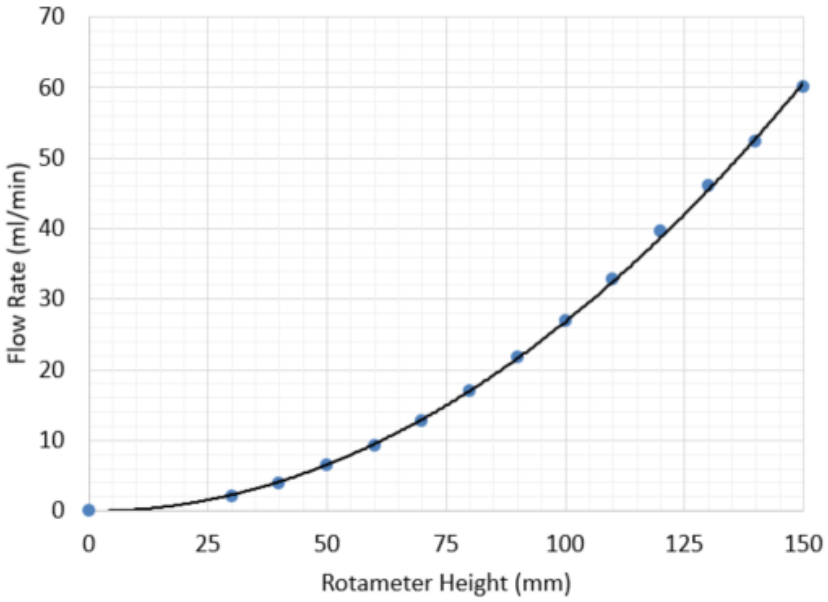

Figure 5. Rotameter calibration curve for soybean oil.

3.4 Oils Tested

Before soybean oil was selected as the primary fluid of interest for this study, white mineral oil and corn oil were tested. White mineral oil is a petroleum-based product that is commonly used in health and beauty products like lotions. Industrially, it is used as a lubricant and as a heat transfer fluid. This oil is commonly used as a heat transfer fluid for electrical transformers due to its very high resistivity and good heat transfer properties. Because of its high resistivity, white mineral oil was the first fluid tested with this experimental setup for this investigation. Tests with this oil mostly proved unsuccessful. Atomization was achieved from time to time

with the electrostatic atomization nozzle but with very low charging resulting in inconsistency in performance. Figure 6 shows the atomized spray produced during testing with white mineral oil. Due to this inconsistent performance, white mineral oil was not tested any further for this investigation.

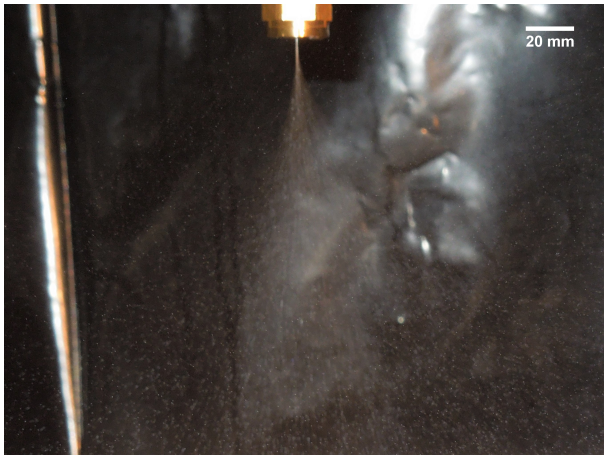

Figure 6. Electrostatic atomization nozzle spraying white mineral oil.

The inconsistent performance with this nozzle and experimental setup with white mineral oil was believed to be due to the very high resistivety of the oil. To validate the test setup and nozzle, corn oil was tested next. Corn oil was investigated previously and successfully atomized with this style of nozzle by Malkawi (1). This oil successfully atomized with consistency using this test setup and the plane-to-plane electrostatic atomization nozzle. Figure 7 shows the

successful atomization of corn oil using this nozzle. The experiment validated the test setup and the nozzle, but since it has already been studied extensively, it was not the focus of this investigation.

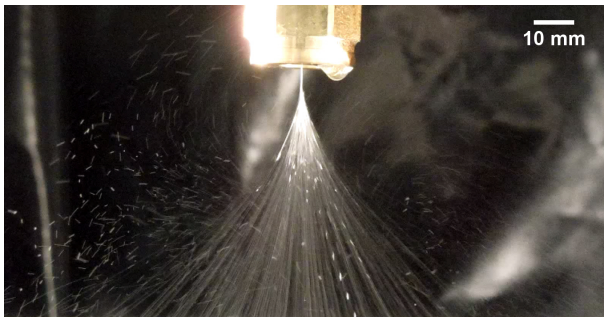

Figure 7. Electrostatic atomization nozzle spraying corn oil.

The electrostatic atomization of pure soybean oil is the focus of this investigation. The research for this thesis was focused on investigating the resulting spray of soybean oil with the plane-to-plane electrostatic atomization nozzle operating at a range of pressures and geometrical conditions. This investigation included analyzing the resulting spray plume geometry, droplet size distribution, and velocity. Both single and multi-orifice configurations of the plane-to-plane electrostatic atomization nozzle were investigated. For all of the experiments conducted, the soybean oil was at ambient temperature. The soybean oil tested was 100% food-grade soybean oil, the properties of which can be found in Table I. The density of the oil was measured using

a pycnometer and was found to be slightly less than that of water. The surface tension was measured using a Kruss K20 tensiometer, and it was found to be about half that of water. The refractive index of the oil was measured using a Reichert AR200 Digital Refractometer. This property was utilized in the setup of the phase Doppler system used to measure droplet size and velocity in this study. Dynamic viscosity was measured using a Brookfield DV-II viscometer. A constant viscosity value was measured for various shear rates demonstrating that the soybean oil is a Newtonian fluid. Distilled water was used as the reference material for the devices mentioned above. Resistivity was derived from a conductivity measurement taken with a D-2, Inc. jet fuel handheld conductivity meter.

TABLE I

PROPERTIES OF SOYBEAN OIL

Property	Value
Density, ρ (g/ml)	0.914
Dynamic Viscosity, μ (cP)	61.0
Surface Tension, σ (dyn/cm)	33.0
Refractive Index, n	1.474
Electrical Resistivity, ρ_e (10^{10} Ωm)	66.7

The performance of the electrostatic atomization nozzle sometimes varied from batch to batch of soybean oil. Initially, the soybean oil was purchased from a grocery store, which was labeled for the grocery store's generic product line. The oil manufacturer was detailed on the label. Several one-gallon bottles of this oil were acquired over a few purchases and used during the single orifice nozzle testing and for some of the multi-orifice nozzle testing. During the single orifice nozzle testing, the spray performance did not change from batch to batch of the oil. However, during the multi-orifice testing, it was observed that the electrical performance of the nozzle spraying a new bottle of soybean oil changed significantly. The oil was much more resistive and required higher voltages to generate the same level of spray specific charge and atomization as had just been tested with the previous batch of oil. It is plausible that the oil from the grocery store's generic product line had been from a different soybean oil manufacturer. For the remainder of the testing, oil was purchased from a bulk supplier in five-gallon bottles. This oil was labeled by the oil manufacturer providing more confidence that the oil would be consistent from batch to batch.

3.5 Spray Characterization Equipment

3.5.1 Standard and High Speed Imaging

The shape and size of the spray plume, as well as the primary modes of atomization, were investigated using various cameras. Images of the spray plume and test setup were taken with a Nikon D7000 DSLR camera with a Nikon Nikkor 24-70 mm f/2.8 lens and a point and shoot Nikon Coolpix camera. Video of the primary breakup mechanism of the electrostatic atomization nozzle was shot using an Olympus i-SPEED TR high-speed imaging (HSI) system

with a Nikon micro-Nikkor 200 mm f/4 lens. The HSI system can acquire videos with a frame rate up to 10,000 fps and with a maximum pixel resolution of 1280 x 1024 up to 2,000 fps. Backlighting was used for HSI testing with the intensity of light into the camera adjusted by the aperture of the lens as well as the frame rate and shutter speed of the camera.

3.5.2 Laser Sheet Imaging

The LaVision SprayMaster system was used to take laser sheet images (LSI) of planer cross sections of the spray. This system consisted of a New Wave Research Solo PIV Nd: YAG dual laser and LaVision Imager Intense camera. The LSI system uses a short-duration pulsed laser that is passed through a diverging lens to generate a laser sheet that illuminates a cross-section plane of the spray. This green, $\lambda = 532$ nm, laser sheet had a Gaussian intensity profile and was about 1 mm thick. A Nikon Nikkor 50 mm f/1.4D lens was used with the Imager Intense camera. This lens allowed for manual adjustment of the aperture and provided the viewing area required to capture the spray plume produced by this nozzle. A band-pass light filter was attached to the lens only allowing the light of the wavelength of the laser to pass through to the CCD sensor of the camera. The liquid droplets scatter the laser light according to the Mie theory where the light intensity is equivalent to the surface area of the droplet. This system was used to evaluate the spray plume geometry quantitatively, and to evaluate the spray distribution qualitatively. The SprayMaster system was calibrated before use by first taking an image of a calibration sheet containing rows and columns of uniformly sized and spaced "+" symbols. The known size and spacing for these markings were entered into the LaVision DaVis 8.1 software to generate a transformation matrix. As is shown in Figure 8, the camera is located at an

off angle from the axis of the spray plume. This correction was performed by the software to transform the skewed, off-axis angle images to a view normal to the laser sheet. The laser sheet Gaussian intensity was corrected by acquiring a set of laser sheet images of the test area filled with a fog of nearly uniform droplet sizes. A stage fog machine was used to generate the fog.

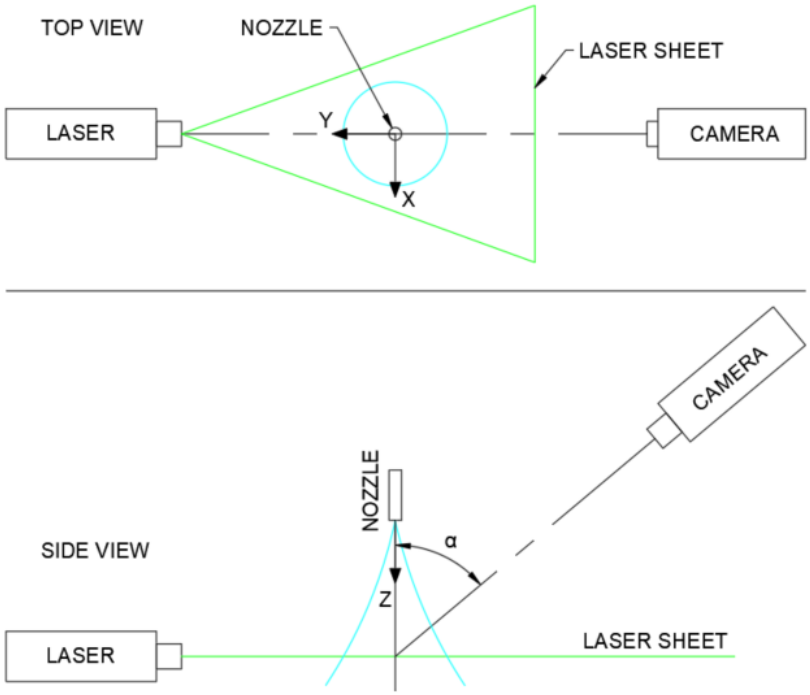

Figure 8. Laser sheet imaging test setup with the LaVision SprayMaster system.

3.5.3 Phase Doppler Interferometry

Drop size and velocity measurements were taken with an Artium PDI-200MD phase Doppler interferometry (PDI) system along with Artium Integrated Management Software (AIMS) version 4.4. This device measures size, velocity in two directions and arrival time for each particle that passes through the measurement volume generated by intersecting laser beam pairs. The PDI was set up with a 500 mm and 1000 mm focal length lenses for the transmitter and receiver respectively, providing a measurable drop size range of 2.6 to 385.6 μm. The receiver was positioned for the 40-degree off-axis forward scatter position as is shown in Figure 9. The primary measurement channel utilized a pair of green, $\lambda = 532$ nm, lasers that measured droplet size and axial velocity in the positive z-direction, denoted by u_z. The second channel used a pair of red, $\lambda = 660$ nm, lasers and measured radial droplet velocity, u_r. The PDI receiver contains three detectors. The AIMS software uses validation criteria for signal to noise ratio, phase comparison, diameter comparison, and others to determine if the signal measured was valid. For example, it analyzes the phase shift of the laser light through the duration of the signal onto the three detectors to determine if it was refracted or reflected light. For the diameter difference validation, it compares the diameter of the droplet based on the light signal detected by the three detectors and compares the diameter difference between the detectors determine if the signal was from an actual droplet. For the PDI testing conducted for this thesis, validation rates ranging between 70% and 94% were achieved. The phase Doppler measurement technique has been well studied and can be further reviewed in publications by Bachalo and Houser (21);

also, the instrument setup and acquisition were performed in a manner similar to that described by Bade and Schick (22).

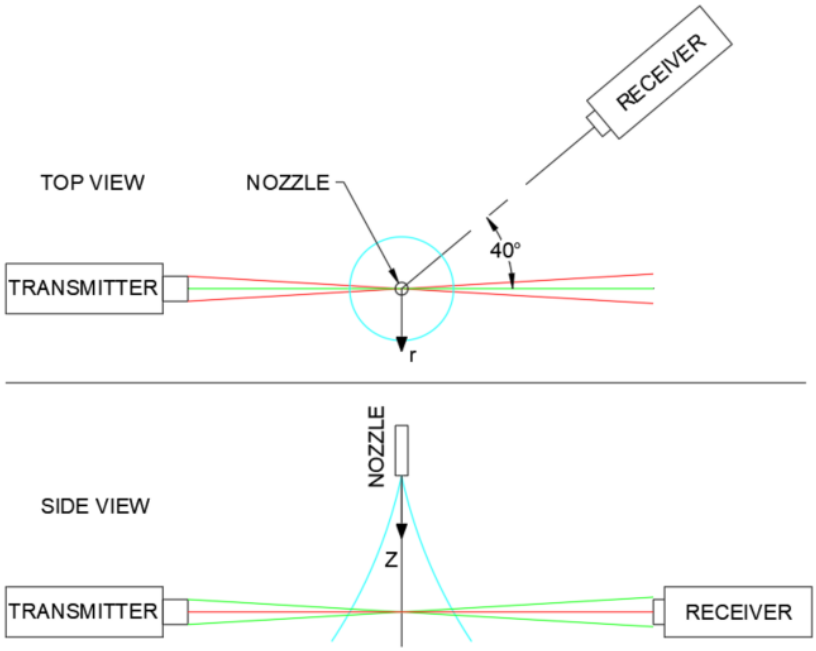

Figure 9. Drop size and velocity test setup using the Artium 2-D phase Doppler interferometry system.

CHAPTER 4

SINGLE ORIFICE ELECTROSTATIC ATOMIZATION NOZZLE TESTING WITH SOYBEAN OIL

The electrostatic atomization nozzle was first experimented with a single orifice configuration while varying the orifice diameter, inter-electrode gap, jet velocity, and nozzle voltage. The ranges that were tested are outlined in Table II. The inter-electrode gap and orifice diameter are illustrated in Figure 3. The inter-electrode gap is presented non-dimensionally, with the orifice diameter as the characteristic length, as L/d. The nozzle was successfully operated at orifice diameters ranging from 100 to 250 microns, but for this study, it was only tested in detail at the diameters of 150 and 200 microns. The jet velocity is the theoretical velocity of the jet at the orifice based on the volumetric flow rate measured by the rotameter and the orifice cross-sectional area shown as

$$u_j = \frac{Q_v}{A}. \tag{4.1}$$

TABLE II

SINGLE ORIFICE NOZZLE TEST CONDITION RANGES.

Property	Range
Orifice Diameter, d (μm)	100 to 250
Inter-Electrode Gap, L/d	0.6 to 1.2
Jet Velocity, u_j (m/s)	10 to 15
Nozzle Voltage, V (kV)	-3 to -10

During the testing of the single orifice, plane-to-plane, electrostatic atomization nozzle with soybean oil, it was observed that the leakage and spray currents never reached a steady state at a given test condition. If all of the nozzle operating conditions were left constant, the spray current and leakage current would gradually increase over time. After an extended period, the spray current would reverse direction and gradually decrease over time. After spraying for a half hour or so, the orifice disk would build up a significant layer of soot or oxidation, which helps explain the eventual decrease in spray current over time. This soot buildup is shown in Figure 10 and was easily wiped off with a swipe of a finger over the surface. In this case, the electrodes of this nozzle are made of tungsten carbide for the high voltage electrode and brass for the grounded orifice disk. These electrode materials appear to be a factor in this suit buildup as more recent designs of this nozzle, not presented in this thesis, use other materials for the electrodes and operate with little to no suit buildup.

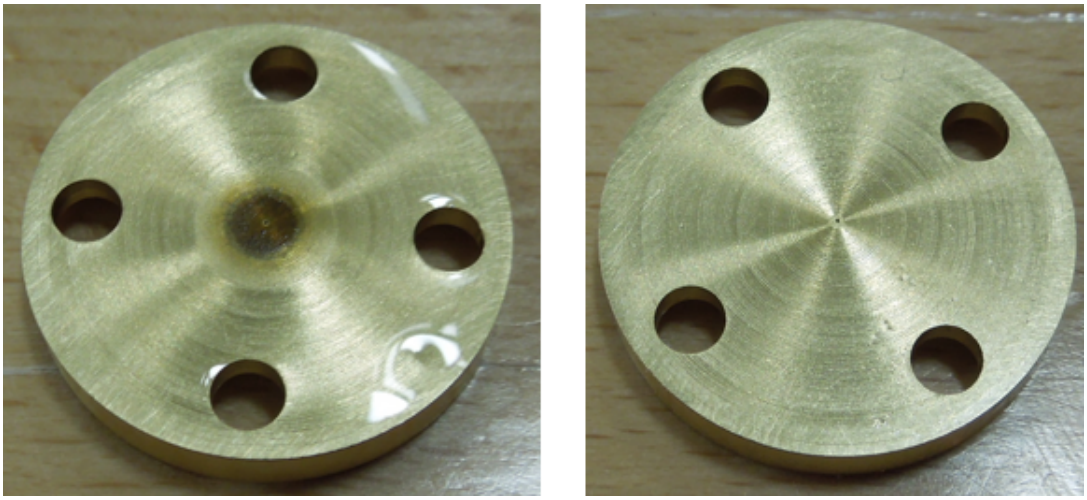

Figure 10. Orifice disk or ground electrode with soot buildup (left) and after cleaning (right).

4.1 Electrical Performance Investigation of the Single Orifice Nozzle

The electrical performance of the electrostatic atomization nozzle was studied for various orifice diameters, d, inter-electrode gaps, L/d, and jet velocities, u_j. The electrical performance was evaluated by calculating the total current,

$$I_t = I_s + I_l, \tag{4.2}$$

injected into the fluid as well as the volumetric spray specific charge,

$$q_v = \frac{I_s}{Q_v} \tag{4.3}$$

or just spray specific charge. The total current is the sum of both the leakage and spray currents whereas the spray specific charge is the ratio of the spray current to the volumetric flow rate of the oil.

The electrical performance results of the single orifice electrostatic atomization nozzle for total current and spray specific charge versus voltage can be found in Figure 11 through Figure 14. Note the stepwise data for spray specific charge results. This is due to the resolution of the digital multimeter used being of the same order of magnitude as the spray current values measured, which is not ideal. The spray specific charge reaches a maximum value before a sudden decrease to a value near, but above, zero. This is called the supercritical breakdown or partial breakdown condition where spray specific charge suddenly decreases but the total current continues to increase unaffected. For this condition, the charging of the oil is unaffected, but the charge escapes to the nozzle body and by corona discharges in the air around the liquid jet before atomization can be generated (10). Visually, partial break down condition is observed when the atomized spray plume collapses to a solid jet of oil. During this investigation, the lights were not allowed to be turned off in the lab where the experiment was conducted, so the corona discharge was not visually observed.

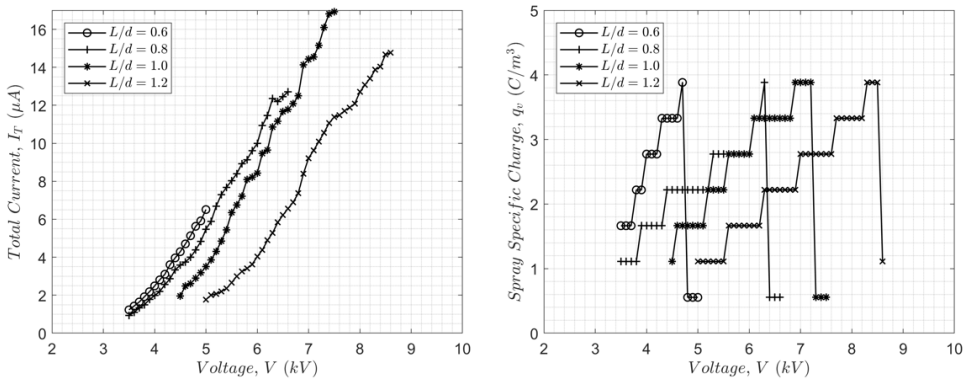

Figure 11. Electrical performance results for the single orifice nozzle operating at $\mathrm{d} = 150\ \mu\mathrm{m}$ and $\mathrm{u_j} = 10\ \mathrm{m/s}$.

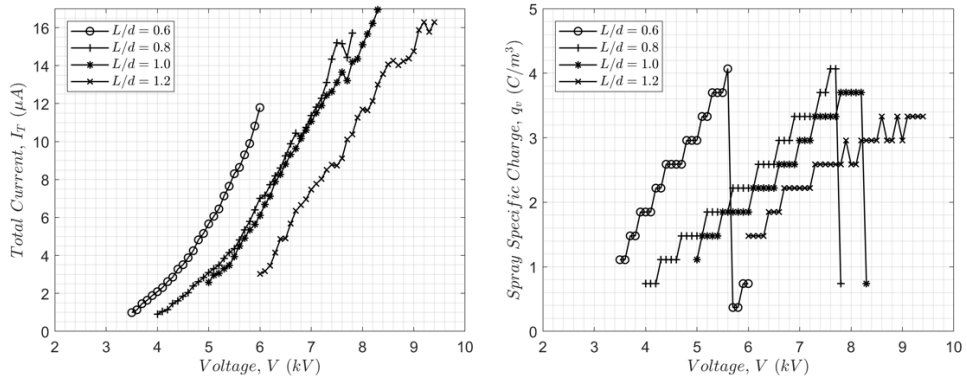

Figure 12. Electrical performance results for the single orifice nozzle operating at $\mathrm{d} = 150\ \mu\mathrm{m}$ and $\mathrm{u_j} = 15\ \mathrm{m/s}$.

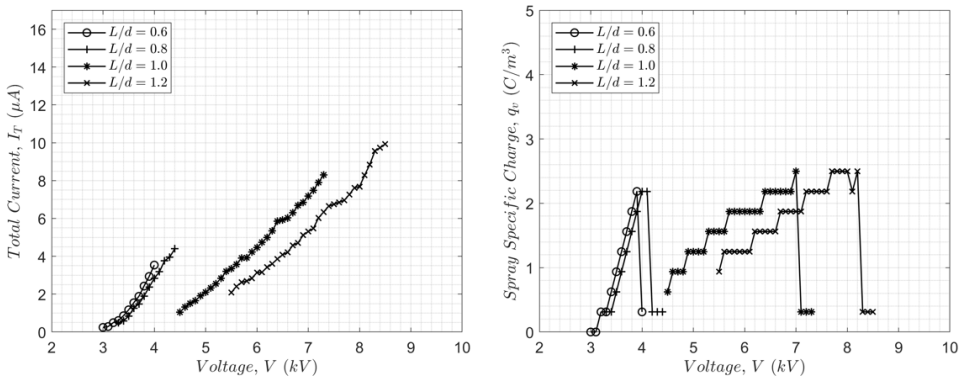

Figure 13. Electrical performance results for the single orifice nozzle operating at $\mathfrak{d} = 200\ \mu\mathfrak{m}$ and $\mathfrak{u}_\mathfrak{j} = 10\ \mathfrak{m}/\mathfrak{s}$.

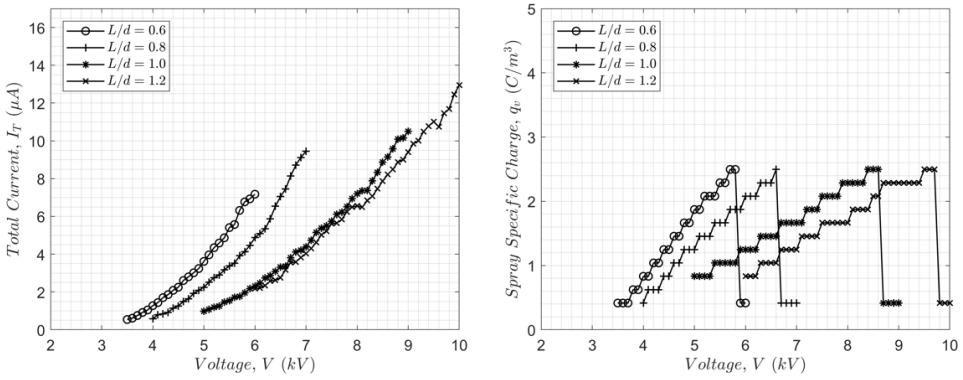

Figure 14. Electrical performance results for the single orifice nozzle operating at $\mathfrak{d} = 200\ \mu\mathfrak{m}$ and $\mathfrak{u}_\mathfrak{j} = 15\ \mathfrak{m}/\mathfrak{s}$.

The inter-electrode gap appears to not effect the maximum spray specific charge for a specific orifice diameter and jet velocity. However, it does impact the operating voltage required to reach the maximum spray specific charge, and it impacts the total current measured from the nozzle. Both the operating voltage and the total current were higher when the maximum spray specific charge was achieved as the inter-electrode gap was increased. An increase in the jet velocity and its associated flow rate reduced the total current and spray specific charge for a given inter-electrode gap and voltage. These results are consistent with observations by previous researchers (10)(11) and by the relationship between electrical field, orifice diameter and spray specific charge given by Equation 2.1.

Table III shows the maximum spray specific charge for the various orifice diameters and jet velocities tested. The jet Reynolds number, given by Equation 4.4, is based on the orifice diameter, d. It is observed that an increase in the jet Reynolds number from a larger jet velocity does not correlate to a change in the maximum spray specific charge obtained. However, an increase in orifice diameter has an effect on the maximum spray specific charge achievable by the nozzle and fluid. The jet Reynolds number alone is not a good correlation to use in the prediction of the maximum spray specific charge performance of an electrostatic atomization nozzle.

$$Re_j = \frac{\rho u d}{\mu} \tag{4.4}$$

TABLE III

MAXIMUM SPRAY SPECIFIC CHARGE RESULTS FOR THE SINGLE ORIFICE NOZZLE ARRANGEMENTS TESTED.

d (μu)	u_j (m/s)	Re_j	$q_{s,max}$ $\left(\frac{C}{m^3}\right)$
150	10	20.7	3.9
	15	31.0	3.8
200	10	27.5	2.4
	15	41.3	2.5

Malkawi (1) conducted electrical performance testing using a point-to-plane electrostatic atomization nozzle with soybean oil. A comparison of the electrical performance between the point-to-plane nozzle to the nozzle used in this study is shown in Figure 15. The point-to-plane nozzle tested by Malkawi generated a significantly lower amount of charge in the oil. The soybean oil he used may have been more resistive than the oil tested in this investigation. In the Oils Tested section, differences in oil properties were observed from batch to batch from this investigation. The larger orifice diameter also results in lower levels of spray specific charge as is observed in the plane-to-plane electrostatic atomization results from $d = 150$ to $d = 200\ \mu m$. This result agrees with the relationship of spray specific charge and orifice diameter with the maximum electric field strength before partial breakdown equation shown in Equation 2.1. The significantly lower total current injected into the oil with the point-to-plane

nozzle appears to show that this combination results in lower levels of charging than the plane-to-plane electrostatic atomization nozzle. This observation was also noted by Malkawi (1) when he tested various electrode shapes with diesel fuel. In general, the results of this investigation with the plane-to-plane electrostatic atomization closely match the results for soybean presented by Malkawi validating the electrical performance testing conducted for this investigation.

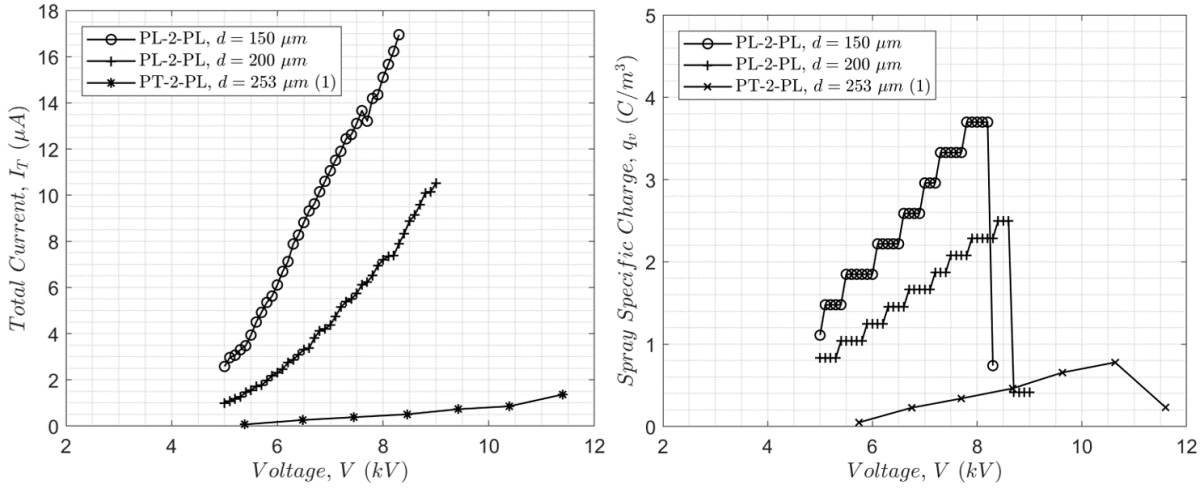

Figure 15. Electrical performance results comparison of the plane-to-plane (PL-2-PL) nozzle to the point-to-plane (PT-2-PL) results from Malkawi for the single orifice nozzle operating at $L/d = 1.0$ and $u_j = 15\ m/s$.

4.2 Spray Plume Characterization of the Single Orifice Nozzle

The characteristics of the spray plume from the single orifice testing were investigated by various imaging techniques. High-speed imaging was used to study the primary modes of atomization with this nozzle. Figure 16 shows the primary breakup mechanism for the electrostatic atomization nozzle. Perturbations develop in the oil jet that exits the nozzle, which moves the charges on the surface of the jet closer to each other. The mutual repulsion of the like charges bends the liquid jet forming the expanding helical pattern. Eventually, the helical jet stretches too far resulting in necking, ligament formation, and atomization into droplets due to Rayleigh instability. In this test, the spray plume was fully atomized within about 25 mm (1 in) from the nozzle. This distanced varied between tests depending on the amount of charge generated in the fluid. It would take several inches from the nozzle for full atomization at low levels of charging. At high levels of charging, the oil appears to be atomized before exiting the orifice.

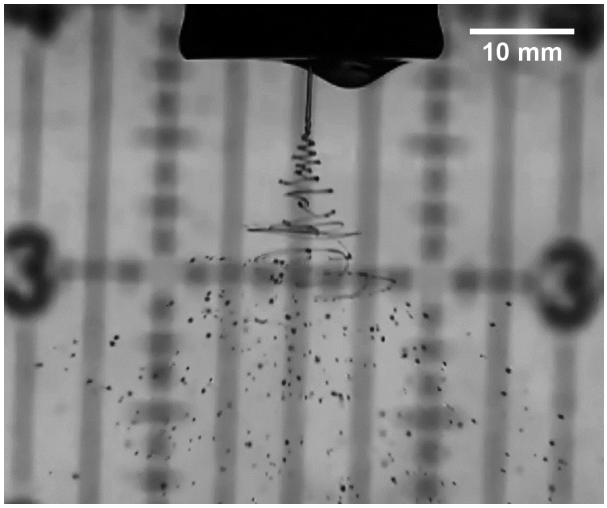

Figure 16. High speed imaging of the single orifice nozzle with $d = 150\mu m$ and $L/d = 0.8$ operating at $u_j = 10m/s$ and $q_v = 2.2C/m^3$ recorded at 5,000 fps.

The image of the spray plume shown in Figure 17 was taken with a DSLR camera and shows that the primary spray plume is in the shape of a cone. As the droplets travel farther from the nozzle, the cone diameter expands. The rate of expansion of the spray plume cone diameter depends on the rate of charge being generated in the oil. If the charging is too high, the spray plume becomes a sphere with droplets traveling in all directions away from the orifice and the nozzle. In Figure 17, small droplets with a high charge to mass ratio exit the spray plume in a direction nearly perpendicular to the primary spray plume. These droplets drift slowly and easily get entrained in the air currents in the lab. If the air is still in the lab, the

small droplets follow the electric field lines from the negatively charged spray plume back to the grounded body of the nozzle. These droplets collect on the nozzle body and other surfaces around the nozzle making it essential that nearby surfaces be grounded to prevent unexpected static buildup and discharges. Some of these droplets are satellite droplets generated during Rayleigh breakup. These small droplets may also be the product of secondary atomization with small, highly charged droplets breaking off of larger droplets. This was not captured during testing but is believed to be possible since small droplets are ejected from the primary spray plume far below the nozzle where satellite droplets should have all escaped. From this testing with soybean oil, the small droplets could not be eliminated but could be significantly reduced by lowering the voltage. When the nozzle is operating near maximum spray specific charge, it is generating a significant amount of these small, highly charged droplets.

Figure 17. Single orifice electrostatic atomization nozzle operating with $d = 200\ \mu m$ and $L/d = 1.0$ at $u_j = 10\ m/s$ and $q_v = 2.2\ C/m^3$.

Laser sheet imaging was conducted at various distances from the nozzle. Fifteen hundred images were taken, averaged into a single image, corrected for the Gaussian intensity of the laser sheet, and then corrected for the camera angle. This was done at several distances of the nozzle producing the sliced results in Figure 18. The laser sheet imaging results confirm that the electrostatic atomizer makes a full cone spray pattern as was expected from the images of the spray plume generated by this nozzle in Figure 16 and Figure 17. At a distance of 40 mm from the nozzle, the spray plume was very concentrated as is shown by the dark red in the center of the spray. Note, the green trail above the primary spray plume in this figure (in the +y region around x=0) is due to the illumination of the spray plume above the laser sheet due to the scattering of the laser sheet light. Also, note the small red data outside of the primary spray plume in the lower right portion of the $z = 40$ mm results, this is noise from dead pixels in the camera that was not filtered out of the data. At further distances from the nozzle, the spray plume expands and becomes less dense. The small droplets generated by secondary atomization are not easily captured by the LSI system, but the very faint outer-spray is primarily made up of these droplets. Small droplets have a small surface area, hence, did not scatter as intense of light on the camera as the larger droplets did.

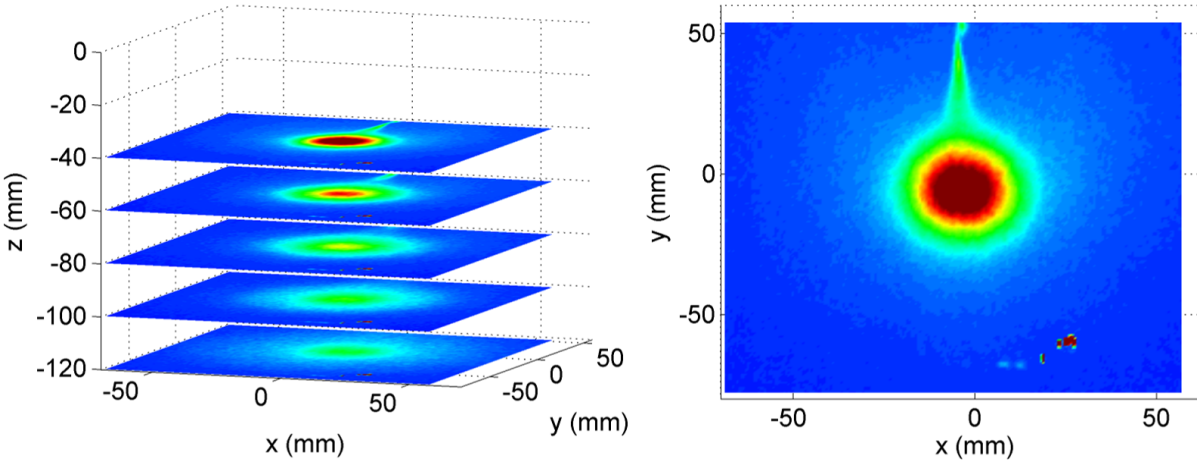

Figure 18. LSI results for the single orifice nozzle with $d = 200\mu m$ and $L/d = 0.8$ while operating at $u_j = 10 m/s$ and $q_v = 1.2 C/m^3$ at various distances (left) and at $z = 40$ mm (right) from the nozzle.

Measurements for droplet size and velocity in two dimensions were taken using a PDI system for the single orifice electrostatic atomization nozzle. Since the nozzle produced a full cone spray plume, point measurements were taken radially from the center to the edge of the spray plume along a single axis as is shown in the schematic in Figure 19. At least 5,000 validated samples were acquired at each measurement point to make up the drop size and velocity statistics for this investigation.

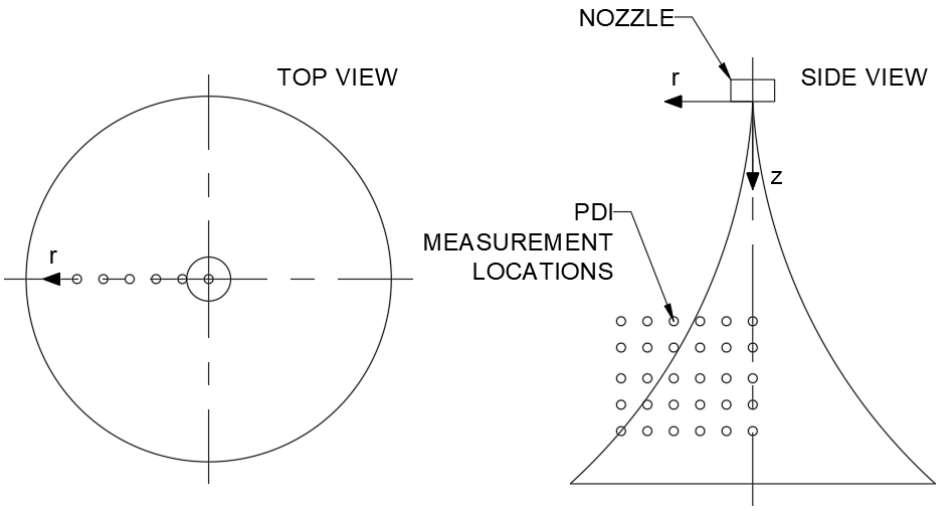

Figure 19. PDI testing locations for the single orifice nozzle.

The results for this testing are shown in Figure 20 through Figure 23. The arithmetic mean diameter, D_{10}, mean volume diameter, D_{30}, and the Sauter mean diameter, D_{32} are plotted versus radial position from the center of the spray for the conditions tested. The drops size, D, spray distance, z, and the radial position, r, were all normalized by the orifice diameter, d. PDI testing was conducted for orifice diameters of 150 and 200 μm and jet velocities of 10 and 15 m/s, all at an inter-electrode gap of $L/d = 0.8$ with the nozzle operating at a constant spray specific charge. As was discussed previously, over time, the spray specific charge would change depending on the soot buildup on the orifice disk. The voltage to the nozzle was adjusted as

the spray current changed during the PDI testing to maintain a constant spray specific charge and spray plume shape.

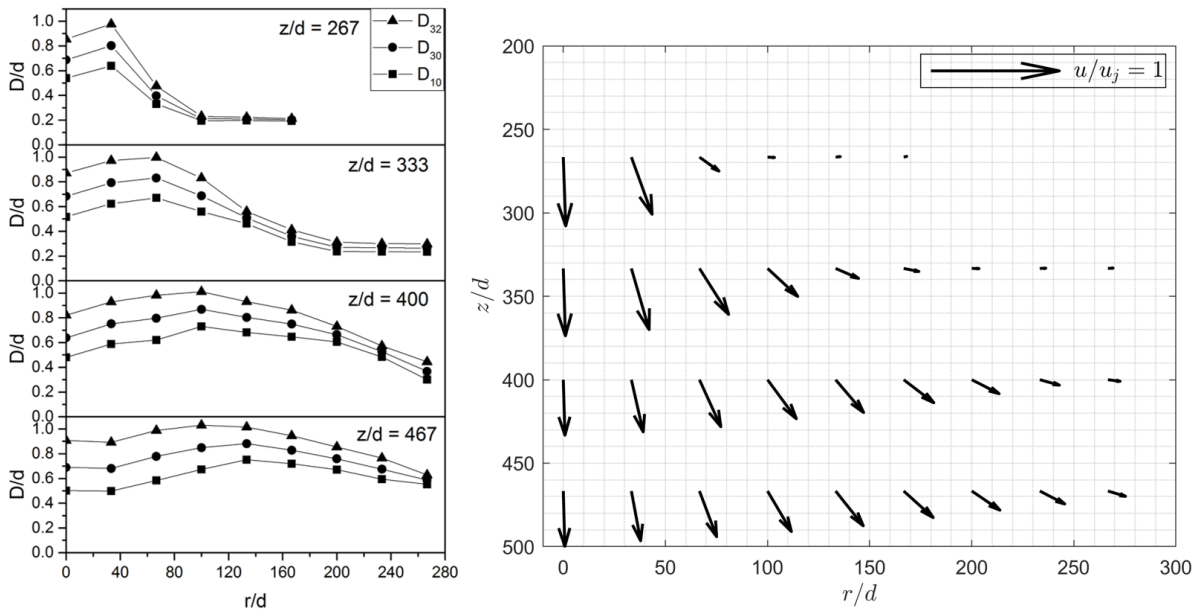

Figure 20. Drop size statistics (left) and average velocity (right) for the single orifice nozzle operating at $d = 150\mu m$, $L/d = 0.8$, $u_j = 10 m/s$ and $q_v = 2.8 C/m^3$.

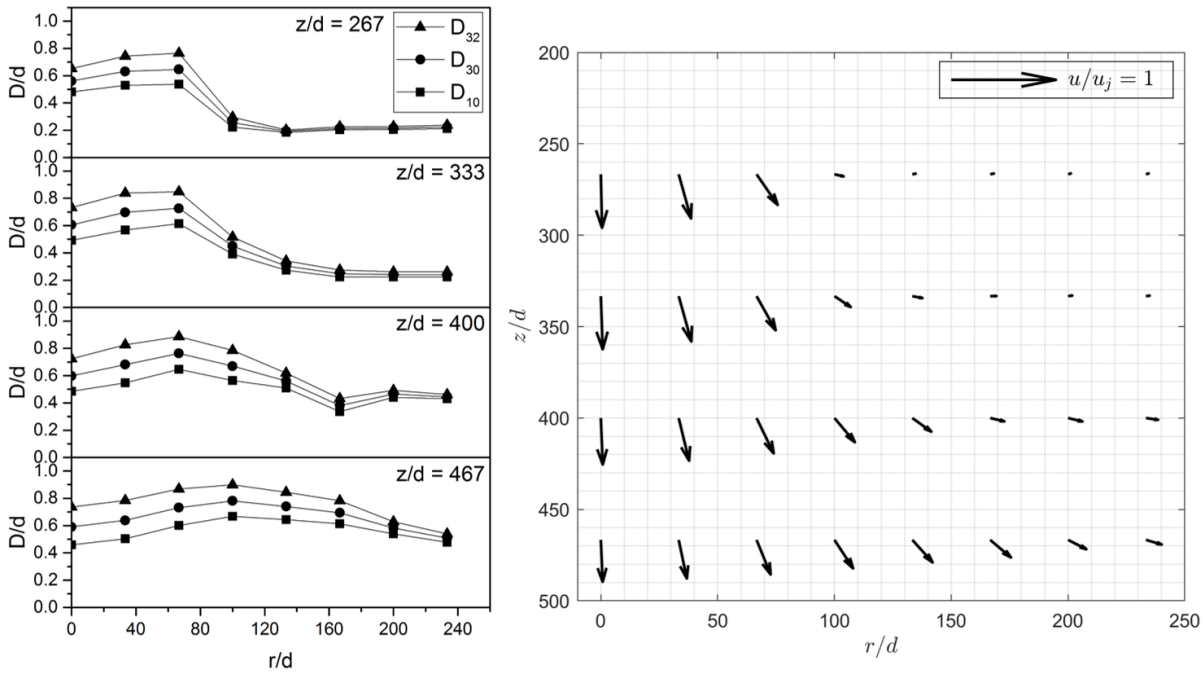

Figure 21. Drop size statistics (left) and average velocity (right) for the single orifice nozzle operating at $d = 150\mu m$, $L/d = 0.8$, $u_j = 15 m/s$ and $q_v = 2.8 C/m^3$.

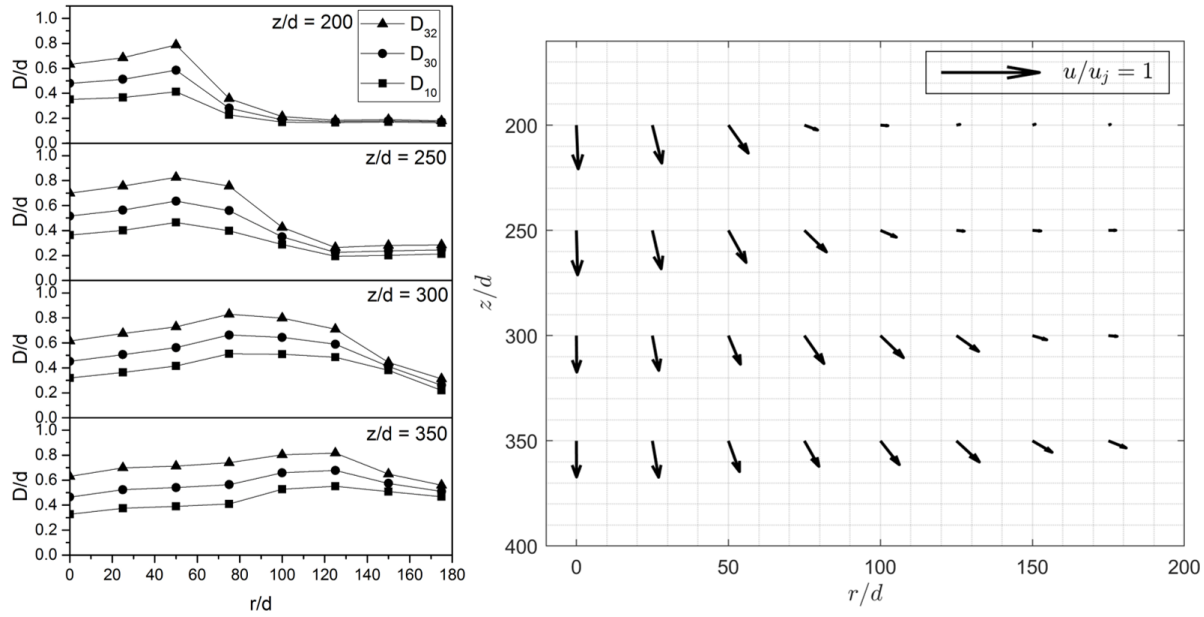

Figure 22. Drop size statistics (left) and average velocity (right) for the single orifice nozzle operating at $d = 200\mu m$, $L/d = 0.8$, $u_j = 10 m/s$ and $q_v = 2.2 C/m^3$.

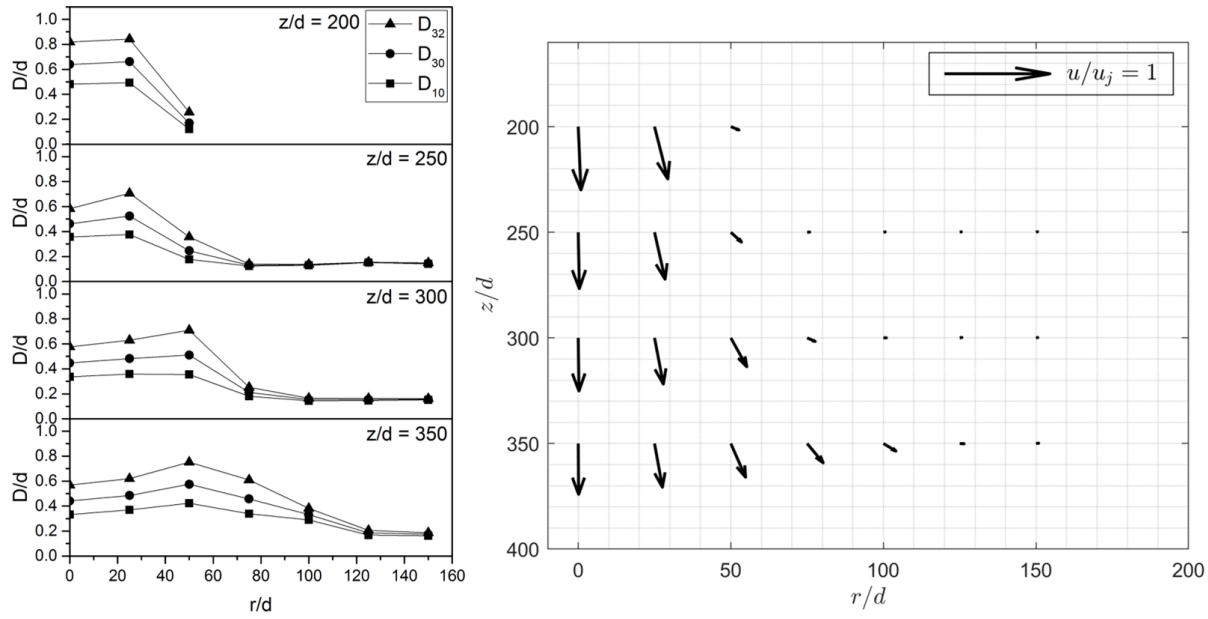

Figure 23. Drop size statistics (left) and average velocity (right) for the single orifice nozzle operating at $d = 200\mu m$, $L/d = 0.8$, $u_j = 15 m/s$ and $q_v = 2.3 C/m^3$.

For the drop size statistics of both orifice diameters and flow rates tested, the curves followed expected trends from what was observed from the HSI and standard image from Figure 16 and Figure 17 respectively. The larger droplets made up the main spray plume while outside the main spray plume resided much smaller and slowly moving droplets. In Figure 20, the D_{32} is the same as the orifice diameter. When the jet velocity is increased, as is shown in Figure 21, smaller droplets were produced. The higher nozzle operating pressure needed to generate the increased jet velocity of this high viscosity oil through such a small orifice diameter added to

the energy of the spray and contributed to the generation of the smaller droplets. When the orifice diameter is increased to 200 μm, nearly the same D_{32} of about 150 μm is measured in the spray plume for the $u_j = 10 m/s$ case. The required pressure to generate this jet velocity is low; the electrical energy injected into the oil is the primary driver of atomization. For all orifice diameters and jet velocities tested, the largest droplets were towards the edge of the spray plume with slightly smaller droplets filling in the center. Tiny droplets drifted from the spray plume to the far-outer regions. For all cases tested, these droplets ranged from about $30 \leq D \leq 40$ μm. The droplets from secondary atomization are not ideal, but the quantity of them can be reduced by lowering the voltage, hence spray specific charge, and are easily captured on grounded, conductive plates or meshing. Figure 24 is a plot of the data rate versus position corresponding to the drop size and velocity results presented in Figure 20. These tiny droplets were few in number compared to the larger droplets in the primary spray plume. Further improvements on the nozzle design and its operation may prevent these small droplets from traveling back to the nozzle as is seen in Figure 17 with the goal of them traveling to the grounded substrate being coated improving the transfer efficiency even further.

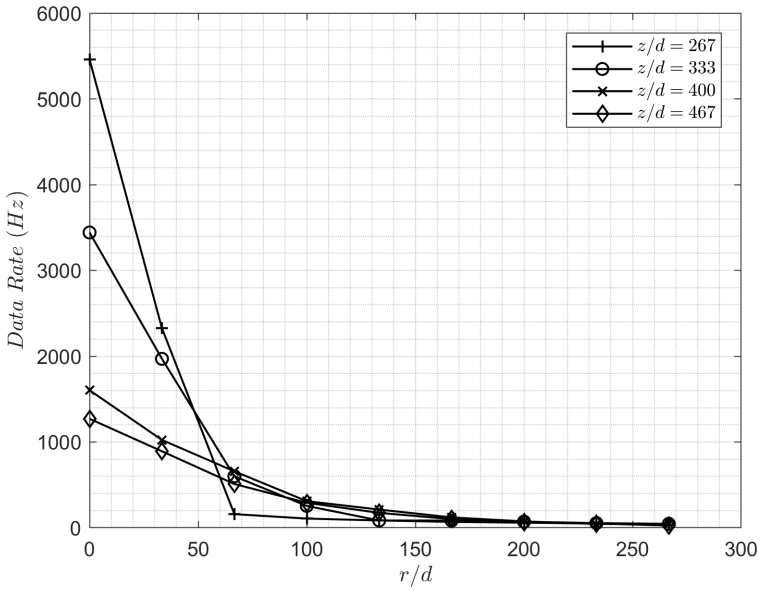

Figure 24. Data rate versus position and spray distance for the single orifice nozzle operating at $d = 150\mu m$, $L/d = 0.8$, $u_j = 10m/s$ and $q_v = 2.8C/m^3$.

The velocity vector fields generated from the 2-D PDI show that the larger droplets within the main spray plume have the largest velocity while the small droplets that escaped the main plume move very slowly. These smaller droplets move away from the spray plume and are carried in air currents and by the electric field generated by the primary spray plume and nozzle. The primary spray plume is well defined by the velocity field plots with the primary plume containing droplets that are moving much faster than the small droplets residing outside. This result supports the imaging results above in that this nozzle produces a full cone spray

plume. The radius of the primary spray plume grows as the spray moves away from the nozzle faster than the linear growth rate experienced from traditional nozzles. This shows that the droplets are imposing a repulsive electrostatic force on each other causing the spray plume radius to accelerate in growth.

Similar drop size trends have been previously published by Shrimpton and Yule (2) for kerosene, properties found in Table IV, operating at $u_{inj} = 10$ m/s, $d = 250$ μm, $q_v = 1.2$ C/m^3. These results are presented in Figure 25. There are two large differences between these tests, which are the viscosity and resistivity of the fluids. For a traditional nozzle operating with hydrodynamic pressure only, it would be expected that the nozzle spraying soybean oil would produce a large drop size distribution than kerosene when operated at the same operating pressure due to the viscosity of the fluids. With the electrostatic atomization nozzle, similar drop size distributions are produced for both soybean oil and kerosene. The difference in resistivity or the other fluid properties may be the reason but it is worth further investigation to determine if there is a viscosity independence on drop size distribution with the electrostatic atomization nozzle as this would be very unique and an important advantage compared to traditional nozzles.

TABLE IV

PROPERTIES COMPARISON OF SOYBEAN OIL AND KEROSENE.

Property	Soybean Oil	Kerosene (7)
Density, ρ (g/ml)	0.914	0.800
Dynamic Viscosity, μ (cP)	61.0	1.1
Surface Tension, σ (dyn/cm)	33.0	23.5
Electrical Resistivity, ρ_e (10^{10} Ωm)	66.7	0.32

The drop size distributions in Figure 25 only overlap away from the center of the spray. The kerosene results show that the drop size distribution is larger in the center of the spray whereas the soybean oil results show the drop size distribution is smaller in the center of the spray. This is believed to be due to the ion mobility between the two fluids. The ion mobility is given by Equation 2.15, which shows that ion mobility is smaller when the viscosity of the fluid is larger. As it was shown in Figure 16, the bending instability produces an expanding helix oil jet until necking and atomization occurs. The charges move slowly through the soybean oil resulting the bulk of the oil moving generating the expanding helix. Yule et al. (7) showed that the primary atomization of white spirit and kerosene was much more chaotic. The atomization of these hydrocarbons consisted of ligaments and droplets ejecting from the sides of the oil jet exiting the nozzle resulting in a core of large droplets in the center of the plume and smaller droplets on the outside of the spray plume. The much lower viscosity of these fluids allowed the charges to move quickly through them. The charges were able to move with low resistance

from the fluid allowing them to eject from the main jet in small fluid droplets leaving the core of large droplets in the center of the spray.

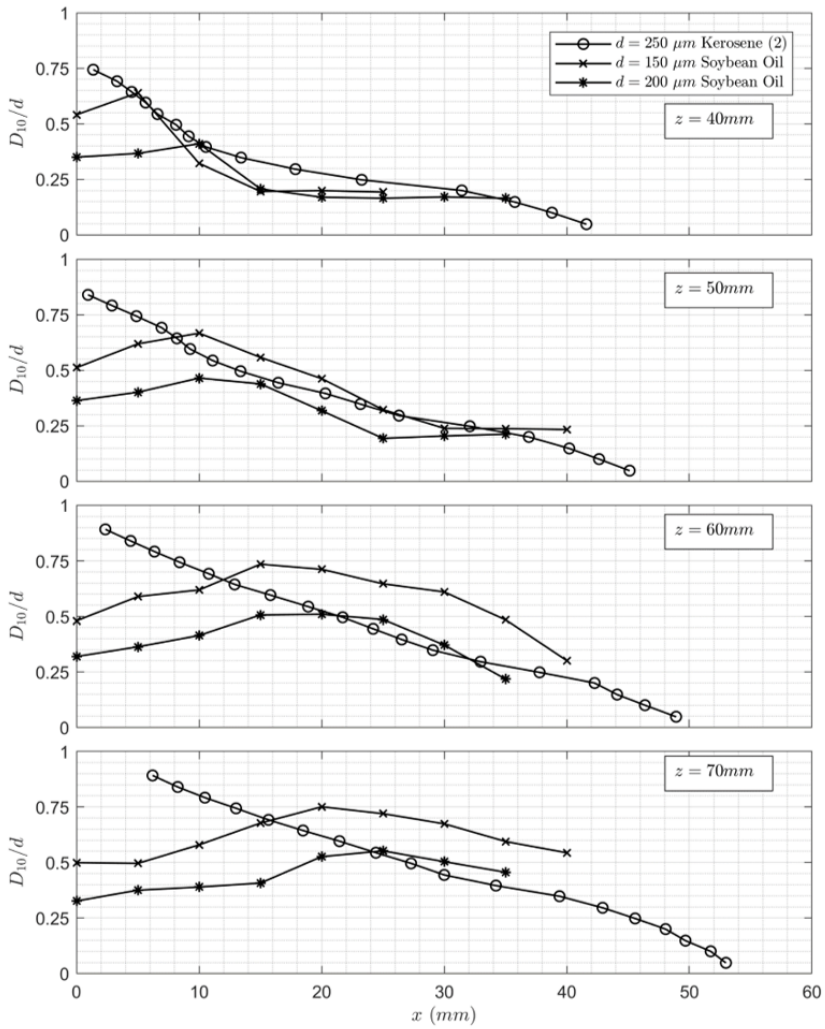

Figure 25. Normalized arithmetic mean diameter, D_{10}/d, for $L/d = 0.8$ and $u_j = 10m/s$.

CHAPTER 5

MULTI-ORIFICE ELECTROSTATIC ATOMIZATION NOZZLE TESTING WITH SOYBEAN OIL

Various multi-orifice configurations were investigated with the plane-to-plane electrostatic atomization nozzle. The motivation to operate the nozzle with multiple orifices was to increase the flow rate and spray coverage it could produce reducing the number of nozzles that would be required to lubricate a production conveyor filled with conductive, grounded substrates. During the investigation of the single orifice nozzle, it was observed that there is a limit to the maximum flow rate achievable while obtaining atomization with the nozzle. Various multi-orifice configurations were investigated to see if the overall flow rate for the nozzle could be increased from what was achievable with the single orifice configuration.

Three orifice configurations were predominately investigated. The first trials were with the orifices located on a circle of the same diameter as the blunt electrode as is shown in Figure 26. The belief is that the charging was strongest in this region due to the sharp radius at the edge of the cylindrical electrode. The spray plume that resulted from this configuration usually had one or two well-atomized plumes and the rest were poorly atomized or remained solid jets. The inconsistency in the charging for each orifice most likely was attributed to the position of the orifices with respect to the electrode. After testing this orifice disk, it was inspected under a microscope, which revealed the actual locations of the orifices. This confirms that one orifice resided outside of the inter-electrode gap resulting in the observed spray plume. The orifices

were drilled using a different machine than that used to make the rest of the orifice disk. The orifice disk was fixed to a two-axis slide table of a small high-speed drill press used to drill the orifices. Each orifice was located on two axes resulting in them being slightly out of their intended position.

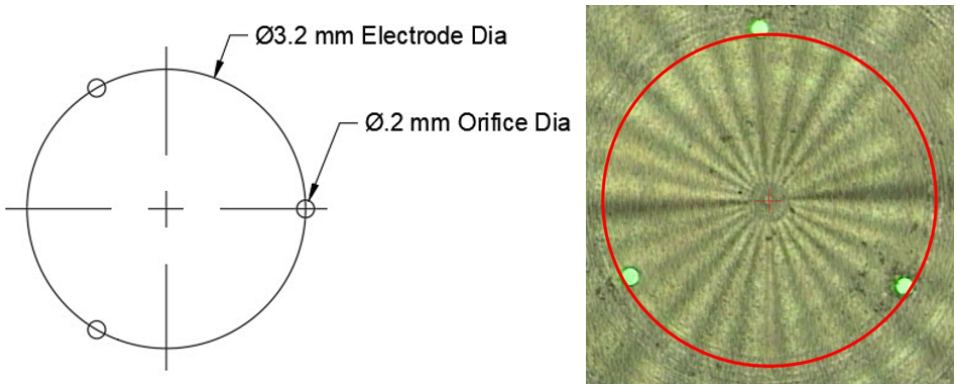

Figure 26. A schematic of the intended three orifice configuration (left) and the actual three orifice configuration produced and tested (right).

To ensure that all of the orifices resided within the inter-electrode gap, a new three orifice configuration was pursued, which had the orifices located on a circle well within the outer diameter of the high voltage electrode. This schematic is shown in Figure 27. This configuration produced more consistent results with all three spray plumes atomizing. This three orifice configuration was used for the testing in the subsequent sections. Another issue that arose was

a more frequent catastrophic breakdown or arcing between the electrodes. While operating this three orifice atomizer for a long duration, the nozzle would randomly and unexpectedly arc. After arcing, the high voltage would be shut off with the oil still flowing through the nozzle. The high voltage would be turned back on and slowly increased until the desired operating voltage. After some time of operation, it would arc again unexpectedly. After a few weeks of operating with this orifice disk with this issue, the orifice disk was observed under a microscope, which revealed that the arcing was occurring in the region between the three orifices. Figure 28 shows the black pits in the brass orifice disk where the arcing occurred. It is possible that the oil that resides in this region becomes trapped and eventually degrades dielectrically resulting in the arcing. Due to this phenomena, this three orifice configuration is not a viable option for an electrostatic atomization nozzle used for an industrial process.

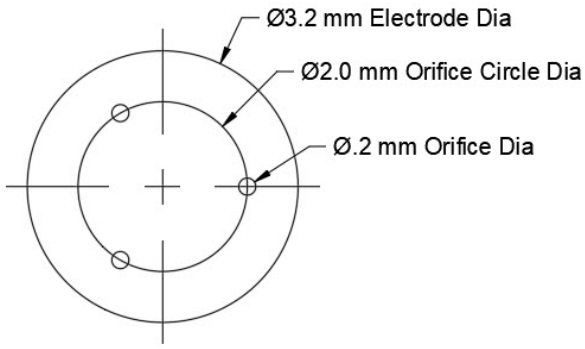

Figure 27. Three orifice configuration with orifices located within the outer diameter of the high voltage electrode.

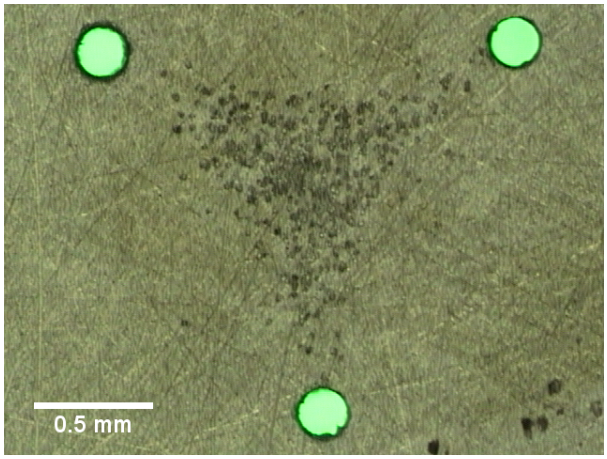

Figure 28. Orifice plate with pitting due to arcing between the electrodes.

5.1 Electrical Performance Analysis of the Multi-Orifice Nozzle

The electrical performance of the multi-orifice electrostatic atomization nozzle was studied for various inter-electrode gap lengths. This testing was done to study how these features affected the charging of the nozzle. The electrical performance was evaluated by plotting the total current, I_T, injected into the fluid as well as the spray specific charge, q_s, versus voltage, V. These values were derived from Equation 4.2 and Equation 4.3 and the measurements for the spray current, leakage current, and volumetric flow rate.

In the Oils Tested section of this chapter, it was discussed that during the electrical performance testing of the multi-orifice nozzle, the oil properties changed from one bottle of oil to the next. Due to this, a new oil supplier was sought, and the electrical performance testing was

redone with this new oil to ensure the results were comparable. Single orifice nozzle tests at the same orifice diameter tested for the three orifice nozzle were conducted with this new oil as well. This is why the results for the single orifice nozzle do not exactly match those presented in the Single Orifice chapter of this thesis.

The results of this testing can be found in Figure 29. As was noted for the single orifice nozzle electrical performance results, the testing for the spray specific charge versus voltage resulted in step-wise results due to the resolution of the digital multimeter used to measure the spray current. It was of the same order of magnitude as the values being measured. In this figure, the total current and spray specific charge are plotted versus voltage for inter-electrode gap distances ranging from 0.6 to 1.2 for both the single and three orifice nozzles. These results show that increasing the inter-electrode gap distance results in lower total current and spray specific charge for a given operating voltage for both the single and three orifice nozzles lower. The total current was nearly equal for both the one and three orifice nozzles, but the spray specific charge was lower. It was expected that the total current would be independent of the number of orifices as it is a function of voltage, inter-electrode gap, and electrode material due to the charging process being an emitter surface phenomenon (12).

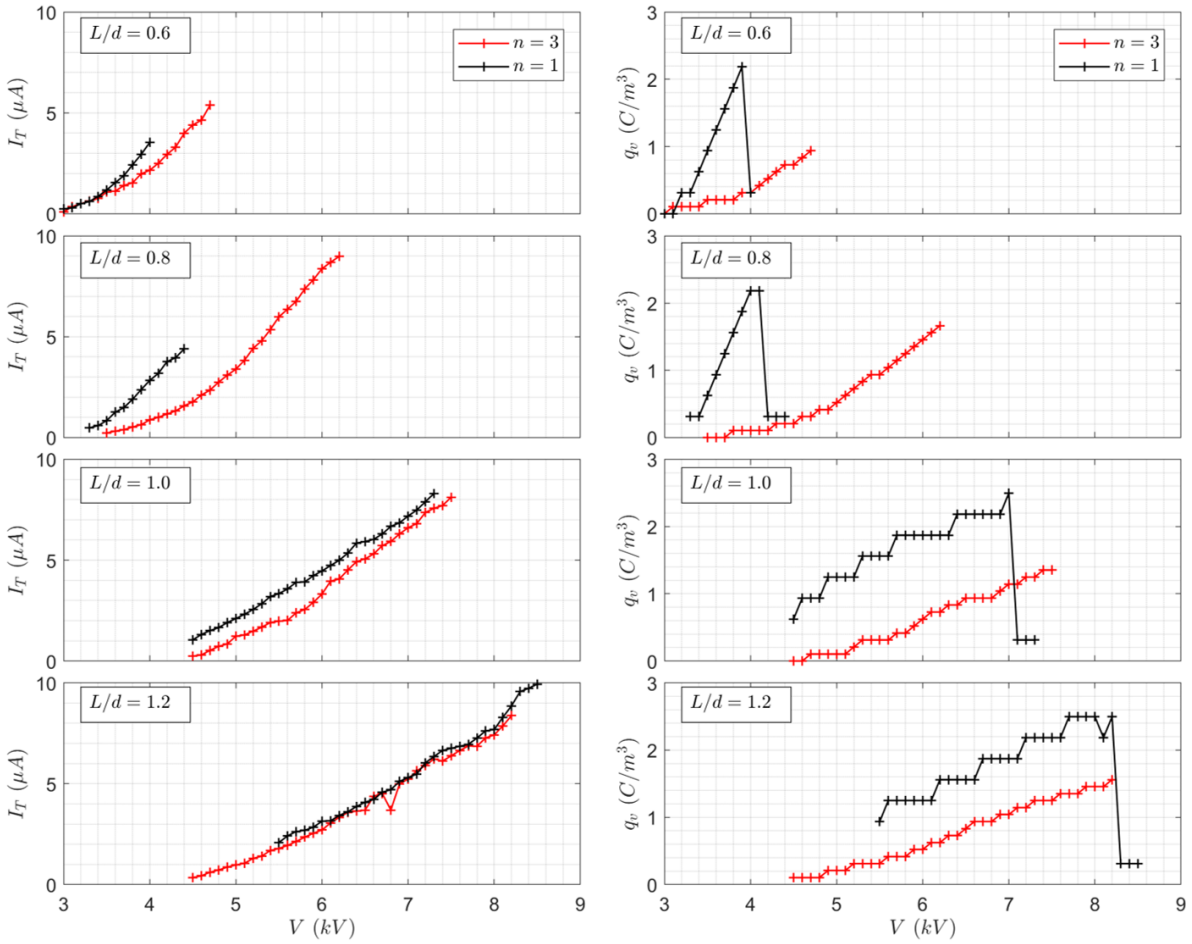

Figure 29. Comparison of a single and three-orifice nozzle for total current (left) and spray specific charge (right) versus voltage with $\mathrm{d} = 200\ \mu\mathrm{m}$ and $\mathrm{u_j} = 10\ \mathrm{m/s}$.

For the single orifice case, the spray specific charge versus voltage resulted in a maximum value achieved before a sudden decrease to a value slightly above zero, which is the partial

breakdown condition discussed previously. As was discussed earlier, arcing occurred unexpectedly during testing. When testing the limits of the electrical performance for the multi-orifice nozzle tested, arcing occurred prior to partial breakdown condition occurring.

The spray specific charge for the three orifice nozzle is much lower than the single orifice nozzle. With the spray specific charge being the ratio of the spray current to the volumetric flow rate of the oil through the nozzle, it is plausible that the spray specific charge would be much less for the three orifice nozzle. However, as it shows in the figures of the next section, atomization is achieved for all three orifices. Figure 30 shows a comparison of spray current versus voltage for the single and three orifice nozzle. This shows that a higher spray current was achieved for the three orifice nozzle versus the single orifice. However, since partial breakdown condition was not achieved for the multi-orifice nozzle, it is not known if triple the spray current can be achieved with the three orifice nozzle versus the single orifice.

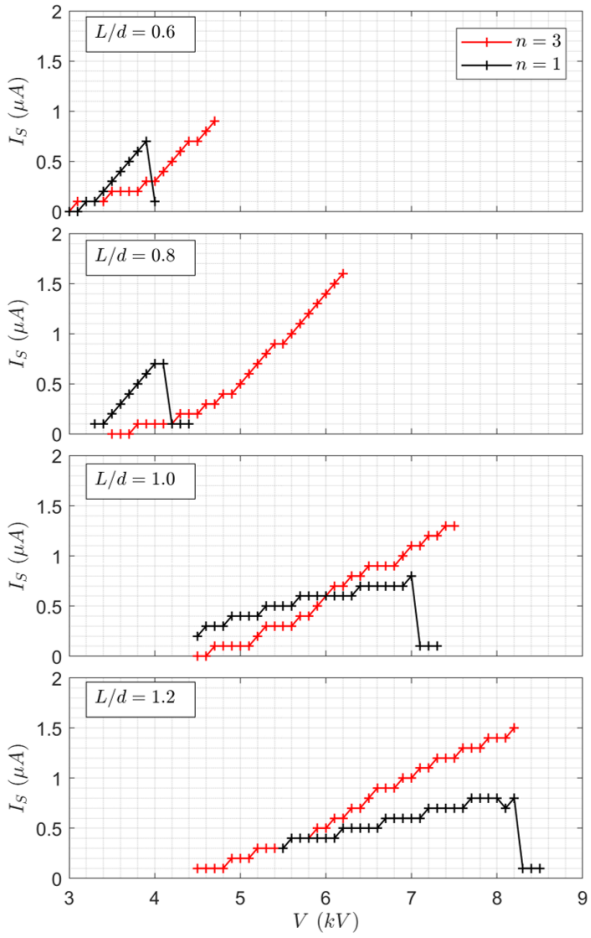

Figure 30. Spray current versus voltage with $\mathrm{d} = 200\ \mu\mathrm{m}$ and $u_j = 10\ \mathrm{m/s}$.

5.2 Spray Plume Characterization of the Multi-Orifice Nozzle

Multi-orifice configurations were investigated via the same imaging analysis noted above for the single orifice nozzle. The characteristics of the spray plume were investigated using a

DSLR and HSI cameras. Figure 31 shows the spray plume from the three orifice nozzle tested and the primary breakup mechanism for the electrostatic atomization nozzle with the orifice size and configuration shown in Figure 27. With zero voltage applied, the three solid jets are nearly parallel to each other. With a large voltage potential applied across the electrodes in the nozzle, perturbations develop in the solid oil jet as they exit the nozzle leading to atomization just as was seen for the single orifice experiments. The charged individual spray plumes initially repel each other generating a wide overall spray plume. Figure 32 shows a larger view of the spray plume generated by the three orifice nozzle. Although the spray plumes initially repel each other, they do overlap further below the nozzle. In Figure 32 smaller droplets can be seen exiting the primary spray plume as was observed during the single orifice testing.

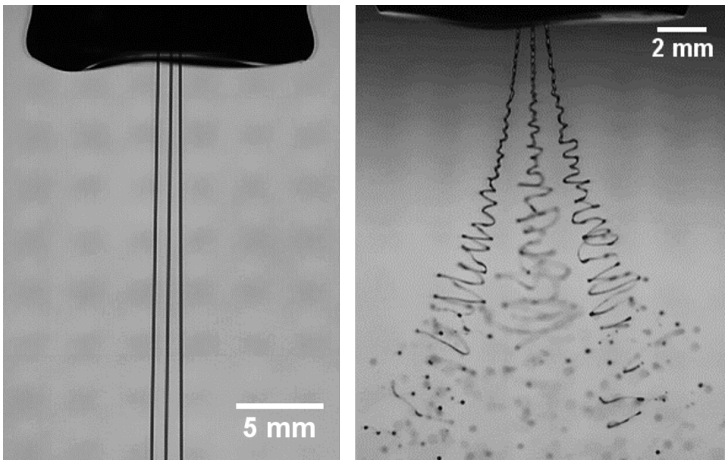

Figure 31. High speed image of the three orifice nozzle operating with no voltage (left), $V = -5.6$ kV (right) and $u_j = 10$ m/s with $d = 200$ μm and $L/d = 1.0$.

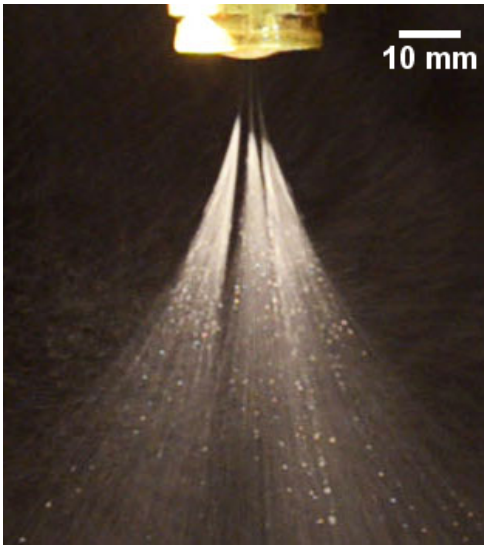

Figure 32. Standard image of the three orifice electrostatic atomization nozzle operating at $V = -5.6$ kV and $u_j = 10$ m/s with $d = 200$ μm and $L/d = 1.0$.

Variability in the performance was observed with the three orifice nozzle used in this study. The three spray plumes were not always balanced as is shown in Figure 33. This figure shows an instance where one spray plume is atomizing aggressively while another is not atomizing until further from the nozzle with a narrower cone angle. This result could be as simple as one orifice being partially plugged or as complicated as how the electroconvection develops from test to test. The unbalanced spray plumes was a fairly regular occurrence resulting in a lack of confidence in the viability of using the multi-orifice electrostatic atomization nozzle, with this design, in an industrial spray process.

Figure 33. Unbalance spray from the three orifice electrostatic atomization nozzle.

The laser sheet imaging results of the three orifice electrostatic atomization nozzle are shown in Figure 34. The LSI results show the three individual spray plumes as was observed in Figure 32. The spray plume widens significantly between the spray distances, z/d, of 625 and 750 from the nozzle. Even at a spray distance of 750 from the nozzle, there are still three distinct spray plumes. At a spray distance of 625, each spray plume has a concentrated core of droplets that tapers to a sparse spray at the edge of each spray plume. At a spray distance of 750, the center core of the spray plume becomes less concentrated. This once again shows that the spray plume is expanding as it is moving away from the nozzle. The like polarity of the excess charge contained within each droplet generates the repulsive force required to generate the full cone spray plume and the force that makes the spray plumes repel each other. Between

these LSI results and the images from above, the multi-orifice electrostatic atomization nozzle is successful in producing a larger flow rate and spray coverage than the single orifice nozzle.

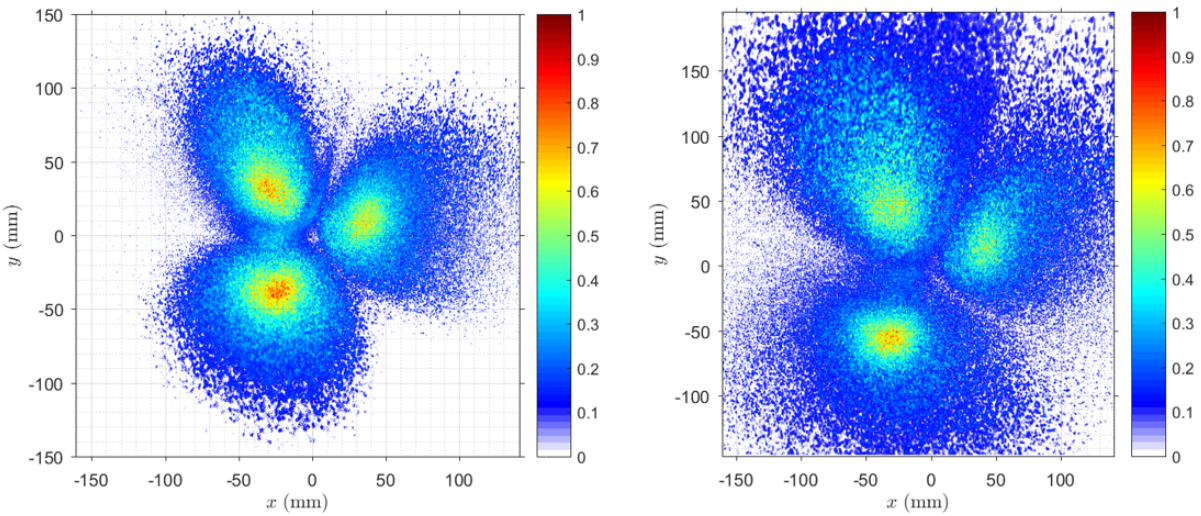

Figure 34. LSI result of the three orifice electrostatic atomization nozzle at $z/d = 625$ (left) and $z/d = 750$ (right) operating at $V = -5.6$ kV and $u_j = 10$ m/s with $d = 200$ μm and $L/d = 1.0$.

Droplet size and velocity testing was also conducted for the three orifice nozzle. Point measurements were taken radially through the center of a spray plume and in between two spray plumes at multiple spray distances as is shown in the schematic in Figure 35. This testing was done similar to that detailed for the single orifice electrostatic atomization nozzle.

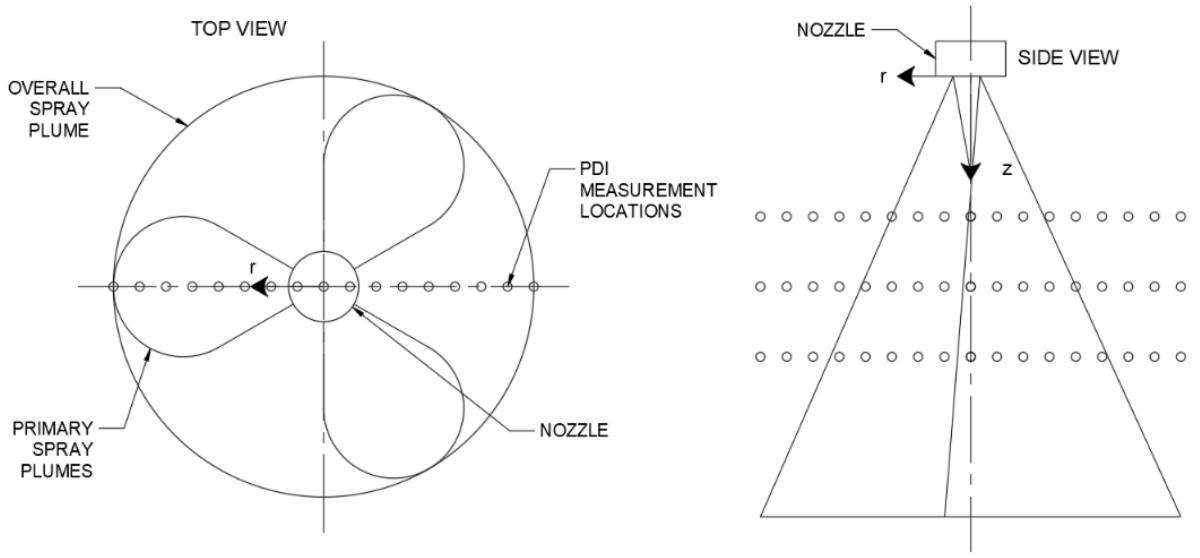

Figure 35. PDI testing locations for the three-orifice nozzle.

The results from the PDI testing are shown in Figure 36 and Figure 37. The arithmetic mean diameter, D_{10}, mean volume diameter, D_{30}, and the Sauter mean diameter, D_{32} are plotted versus radial position for the conditions tested. The drop size, D, spray distance, z, and the radial position, r, were all normalized by the orifice diameter, d and the velocity magnitude by the jet velocity, u_j. Drop size and velocity measurements were taken for a $d = 200\ \mu m$, three orifice nozzle, operating with a $u_j = 10\ m/s$ and an L/d ratio of 1.0 with the nozzle operating steadily at a spray specific charge of 1.2 C/m^3. For the drop size results presented, the center of the overall spray plume is at $r/d = 0$. To the left of zero, measurements were taken through the center of an individual spray plume and to the right between two individual spray

plumes. These measurements were taken at spray distances of $z/d = 500$, 750, and 1000 from the nozzle. The center of the overall spray plume contains mostly tiny droplets from secondary atomization at a spray distance of $z/d = 500$. Some larger droplets mix in with the small droplets at $z/d = 750$. The individual spray plumes are mostly overlapping at $z/d = 1000$, which is evident by the increase in drop size statistics. A larger spray distance should lead to better mixing of the spray plumes and a more even drop size distribution across the overall spray plume. At a spray distance of $z/d = 500$, minimal overlapping of the spray plume is occurring as is evident by all of the drop size statistics being small and nearly the same meaning that the droplets are nearly all the same size. The same is mostly true to the right of $r/d = 0$ at this spray distance. The drop size testing results for soybean oil show that the Sauter mean diameter is nearly the same length as the orifice diameter. This result was also seen in drop size testing of standard UK diesel fuel by Kourmatzis et al. (12), which is 25 times less viscous than soybean oil. Once again, the electrostatic atomization nozzle produces roughly the same drop size distribution regardless of the viscosity of the fluid.

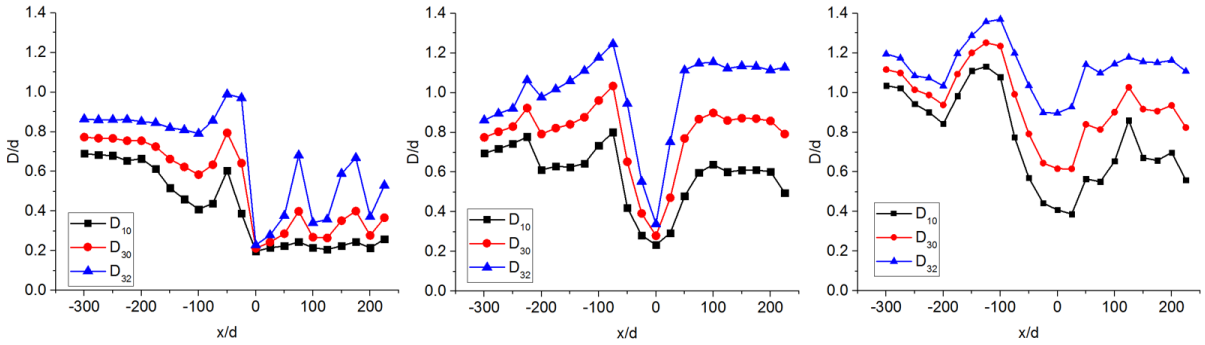

Figure 36. Drop size statistics for a three-orifice electrostatic atomization nozzle with a $u_j = 10 m/s$, $d = 200 \mu m$, $L/d = 1.0$, and $q_v = 1.2\ C/m^3$ at $z/d = 500$ (left), $z/d = 750$ (middle), and $z/d = 1000$ (right).

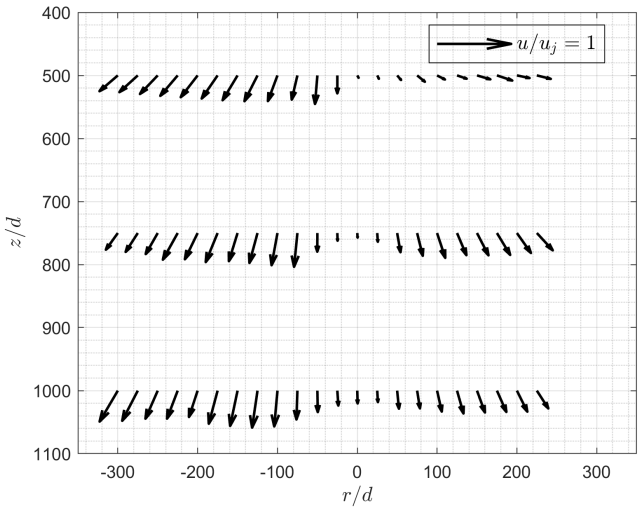

Figure 37. Normalized 2-D velocity (u/u_j) profile for a three-orifice electrostatic atomization nozzle with a $u_j = 10 m/s$, $d = 200 \mu m$, $L/d = 1.0$, and $q_v = 1.2\ C/m^3$.

For the two-dimensional velocity profile shown in Figure 37, it is observed that the center of the overall spray plume contains very slow moving droplets. Previous results for PDI testing of single orifice nozzles showed that the small droplets from secondary atomization outside the main spray plume moved very slowly. The small velocity and drop sizes measured in the center of the overall spray plume at spray distances of z/d of 500 and 750 reinforce that the three spray plumes are not overlapping in the center, however, at a spray distance of 750, the spray plumes do begin to overlap away from the center of the nozzle. This matches what was observed with the drop size results in Figure 36 and the LSI results from Figure 34. The two-dimensional

velocity profile also shows that the droplets inside of an individual spray plume have greater velocity magnitude than those in between two spray plumes.

CHAPTER 6

CONCLUSIONS AND FUTURE WORK

6.1 Conclusions

The motivation for this research was to study and develop the electrostatic atomization nozzle with the goal of developing it for industrial oil coating processes. Spray characterization testing via various imaging techniques including high-speed imaging, laser sheeting imaging, and phase Doppler interferometry were conducted to analyze the spray plume generated by single and multi-orifice electrostatic atomization nozzles with soybean oil. The single orifice nozzle was successful in atomizing soybean oil for a range of orifice diameters and flow rates. The multi-orifice electrostatic atomization nozzle was also successfully tested with soybean oil but with some challenges. Some takeaways from this testing are the following.

- The single orifice electrostatic atomization nozzle spraying soybean oil produced similar drop size statistics away from the center of the spray as that previously published for kerosene. In the center of the spray plume, the kerosene tests resulted in larger drop size distributions due to the difference in how the fluids atomized. Kerosene has about 2% of the viscosity of soybean oil. The viscosity affected the drop size distribution in the center core of the spray, but in the outer portions of the spray plume, there may be a viscosity independence when it comes to the drop size distribution produced by an electrostatic atomization nozzle. For conventional hydraulic or two fluid nozzles, the viscosity of the

fluid being atomized has a great impact on the resulting drop size distribution. This makes the electrostatic atomization and its primary atomization modes of bending and Raleigh instabilities unique. This seeming viscosity independence on drop size distribution requires further investigation.

- The testing of the multi-orifice electrostatics atomization nozzle was successful in increasing the oil throughput of the nozzle and in the increase of spray coverage. The like charged plumes repelled each other initially generating a large spray coverage area on the substrate being sprayed.
- The multi-orifice electrostatic atomization nozzle design tested proved challenging to work with resulting in inconsistent spray performance between tests and unexpected catastrophic breakdown between the electrodes. The inconsistent spray performance was evident by uneven spray plumes produced showing that the spray specific charge levels between the jets of oil exiting the nozzle were not always balanced. This was not measured directly but was evident in the distance from the nozzle where the jets were fully atomized and the cone angles produced. With all of the orifices residing well within the outer diameter of the high voltage electrode, this was more a function of the potential orifices were partially clogged or the function of the electroconvection of the oil between the electrodes. The unexpected catastrophic breakdown between the three orifices suggests that the fluid resided in this region long enough to dielectrically break down. With electrode and orifice configuration tested, it is easy to see how the fluid would get trapped in this region.

6.2 Recommendations for Future Work

Some recommendations for future work ideas are the following.

- Conduct drop size testing with the single orifice, plane-to-plane, electrostatic atomization nozzle with other resistive fluids. This testing would help support or debunk the viscosity independence for drop size distribution resulting from the electrostatic atomization nozzle observed in this thesis.
- Redesign the electrostatic atomization nozzle to better support the incorporation of multiple orifices in the nozzle. Work would need to be done to prevent areas where the fluid would be stagnant between the electrodes, which leads to catastrophic breakdown within the nozzle. New designs should not only aim to stabilize the performance of the electrostatic atomization system, but to also continue to push the limits on maximum flow rate and spray coverage from a single nozzle to provide the flexibility required to be integrated into various industrial oil coating processes.

CITED LITERATURE

1. Malkawi, G.: Point-To-Plane and Plane-to-Plane Electrostatic Charge Injection Atomization for Insulating Liquids. Ph.d. thesis, University of Illinois at Chicago, 2009.

2. Shrimpton, J. and Yule, A.: Characterization of charged hydrocarbon sprays for application in combustion systems. Experiments in Fluids, 26(5):460–469, 1999.

3. Melcher, J. and Taylor, G.: Electrohydrodynamics: A review of the role of interfacial shear stresses. Annual Review of Fluid Mechanics, 1:111–146, 1969.

4. Kim, K. and Turnbull, R.: Generation of charged drops of insulating liquids by electrostatic spraying. Journal of Applied Physics, 47(5):1964–1969, 1976.

5. Robinson, K., Turnbull, R., and Kim, K.: Electrostatic spraying of liquid insulators. IEEE Transactions on Industry Applications, IA-16(2):308–317, 1980.

6. Kelly, A.: Electrostatic Atomizing Device, US Patent 4,255,777, 10 Mar 1981.

7. Yule, A., Shrimpton, J., Watkins, A., Balachandran, W., and Hu, D.: Electrostatically atomized hydrocarbon sprays. Fuel, 74(7):1094–1103, 1995.

8. Shrimpton, J. and Yule, A.: Atomization, combustion, and control of charged hydrocarbon sprays. Atomization and Sprays, 11:365–396, 2001.

9. Rigit, A. and Shrimpton, J.: Electrical performance of charge injection atomizers. Atomization and Sprays, 16:401–419, 2006.

10. Shrimpton, J. and Mashayek, F.: Electrostatic atomization and combustion of electrically insulating liquids. In 47th AIAA Aerospace Sciences Meeting Including The New Horizons Forum and Aerospace Exposition, Orlando, FL, January 2009.

11. Lehr, W. and Hiller, W.: Electrostatic atomization of liquid hydrocarbons. Journal of Electrostatics, 30:433–440, 1993.

12. Kourmatzis, A., Allen, J., and Shrimpton, J.: Electrical and spray characteristics of a multi-orifice charge-injection atomizer for electrically insulating liquids. Atomization and Sprays, 20(4):269–280, 2010.

13. Kourmatzis, A.: Pulsed Charge Injection Atomization and Turbulent Electrohydrodynamics. Ph.d. thesis, Univerisity of Southampton, 2011.

14. Ergene, E.: Investigation of the Electrostatic Atomization Method for Remote Injection and High Pressure. Ph.d. thesis, University of Illinois at Chicago, 2012.

15. Shrimpton, J.: Charge Injection Systems, Physical Principles, Experimental and Theoretical Work. Berlin, Springer, 2009.

16. Castellanos, A.: Basic concepts and equations in electrohydrodynamics. Course and Lectures-International Centre for Mechanical Sciences, 1(380):1–82, 1998.

17. Sankaran, A., Staszel, C., Sahu, R., Yarin, A., and Mashayek, F.: Evidence of faradic reactions in electrostatic atomizers. Langmuir, 33(6):1375–1384, 2017.

18. Castellanos, A.: Coulomb-driven convection in electrohydrodynamics. IEEE Transactions on Electrical Insulation, 26(6):1201–1215, 1991.

19. Atten, P.: Electrohydrodynamic instability and motio induced by injected space charge in insulating liquids. IEEE Transactions on Dielectrics and Electrical Insulation, 3(1):1–17, 1996.

20. Kourmatzis, A. and Shrimpton, J.: Electrohydrodynamic inter-electrode flow and liquid jet characteristics in charge injection atomizers. Experiments in Fluids, 55(3), 2014.

21. Bachalo, W. and Houser, M.: Phase/doppler spray analyzer for simultaneous measurements of drop size and velocity distributions. Optical Engineering, 23(5):583–590, 1984.

22. Bade, K. and Schick, R.: Phase doppler interferometry volume flux sensitivity to parametric settings and droplet trajectory. Atomization and Sprays, 21(7):537–551, 2011.

VITA

Education

M.S. in Mechanical Engineering — 08/2013 to 12/2017
University of Illinois at Chicago
Chicago, IL, USA

B.S. in Mechanical Engineering — 08/2011 to 05/2013
University of Illinois at Chicago
Chicago, IL, USA

A.E.S Associates in Engineering Science — 08/2009 to 05/2011
College of DuPage
Glen Ellyn, IL, USA

Professional Experience

Spraying Systems Co. — 05/2013 to Present
Research Engineer

- Quote, design and test prototype spray systems. Involves writing project proposals, following Spraying Systems Co. design standards and processes, ECOs, assisting manufacturing with the planning and tooling to machine the components and testing the prototypes for safety, function and performance.
- Quote and conduct testing for outside customers for drop size analysis, conveyorized optimization investigations, rheology and sprayability investigations and proof of concepts. Involves working with many different measurements systems for drop size and velocity analysis, i.e. phase Doppler particle analyzers, laser sheet imaging, laser diffraction analyzers. Each test involves a custom setup, calibration validation, testing and writing a technical report.
- Design, install and validate equipment and systems for the research lab. This includes equipment and PLC controlled systems with heaters, pumps, flow meters, pipes, valves and sensors.

UTC Aerospace Systems — 05/2012 to 01/2013
Manufacturing Engineer Intern

- Designed fixtures and tooling to aid in manufacturing and assembly of aerospace pumps and gear boxes.
- Developed and implemented an automated system for the pressurizing and baking procedure for the curing process of custom carbon seals.
- Updated Job Instruction Sheets for the assembly of pumps and gearboxes.

- Analyzed pumps and their components that were test rejects to determine the cause of the test failure and developed the rework procedure.
- Updated production order routings for test and quality reject units.
- Determined the cause of repeat test rejects and developed a plan of correction. Plan included new tooling, updates and clarification of Job Instruction Sheets, and training procedures to correct the issues leading to the repeat rejects.